Nitrogen incorporation in silicates and metals: Results from SIMS, EPMA, FTIR, and laser-extraction mass spectrometry

Article *in* American Mineralogist · January 2019

DOI: 10.2138/am-2019-6533

CITATIONS
3

READS
186

7 authors, including:

Anette von der Handt
University of Minnesota Twin Cities
69 PUBLICATIONS **611** CITATIONS
SEE PROFILE

Evelyn Füri
Centre de Recherches Pétrographiques et Géochimiques
44 PUBLICATIONS **508** CITATIONS
SEE PROFILE

Celia Dalou
Centre de Recherches Pétrographiques et Géochimiques
33 PUBLICATIONS **223** CITATIONS
SEE PROFILE

George R Rossman
California Institute of Technology
478 PUBLICATIONS **13,796** CITATIONS
SEE PROFILE

American Mineralogist, Volume 104, pages 31–46, 2019

Nitrogen incorporation in silicates and metals: Results from SIMS, EPMA, FTIR, and laser-extraction mass spectrometry

Jed L. Mosenfelder[1,*], Anette Von Der Handt[1], Evelyn Füri[2], Celia Dalou[1,2], Richard L. Hervig[3], George R. Rossman[4], and Marc M. Hirschmann[1]

[1]Department of Earth Sciences, University of Minnesota, 150 Tate Hall, Minneapolis, Minnesota 55455, U.S.A.
[2]Centre de Recherches Pétrographiques et Géochimiques, CNRS-UL, 54501 Vandœuvre-lès-Nancy, France
[3]School of Earth & Space Exploration, Arizona State University, Tempe, Arizona 85287-1404, U.S.A.
[4]Division of Geological and Planetary Sciences, California Institute of Technology, M/C 170-25, Pasadena, California 91125-2500, U.S.A.

Abstract

A quantitative understanding of nitrogen incorporation in Earth materials is important for constraining volatile evolution in planetary bodies. We used a combination of chemical (SIMS, EPMA, and laser-extraction mass spectrometry) and spectroscopic (FTIR) observations to study nitrogen contents and speciation mechanisms in silicate glasses, metal alloys, and an N-bearing silicate mineral (hyalophane). One suite of Fe-free basaltic glasses was studied by all four methods. Concentrations of N in these glasses determined by EPMA are systematically higher than those measured by laser extraction but agree within mutual 2*s* uncertainties, demonstrating the general veracity of the EPMA method. SIMS working curves based on measurement of $^{14}N^+$ and $^{14}N^{16}O^-$ as a function of N content determined by EPMA (or laser extraction) are best fit with exponential functions rather than the linear regressions that are most commonly applied to SIMS data. On the other hand, the relationship based on $^{12}C^{14}N^-$ for C-poor, Fe-free glasses is exceptionally well fit to a linear regression ($r^2 = 1$, $p < 0.001$), in contrast to expectations from previous work on glasses with lower N contents. Matrix effects on the SIMS signals associated with Fe or H_2O content are not justified by the data, but volatile data (both N and H) for hyalophane, which contains 20 wt% BaO, reveal matrix effects possibly induced by its high average molar mass. A combination of FTIR and chemical data, together with a thorough review of the literature, was used to determine incorporation mechanisms for N in the Fe-free glasses. We infer that under reducing conditions at high pressure and temperature N is dissolved in basaltic melts chiefly as NH_2^- and NH^{2-}, with N_2 and/or nitride ($X\text{-}N^{3-}$) complexes becoming increasingly important at low f_{O_2}, increasing N content, and decreasing H content. Our results have implications for future studies seeking to accurately measure N by SIMS and for studies of N partitioning at high pressure relevant to planetary accretion and differentiation.

Keywords: SIMS, nitrogen, speciation, FTIR, EPMA, bonding, carbon

Introduction

Recent experimental studies have shown that nitrogen can be a significant constituent in deep-seated silicate melts and minerals (Miyazaki et al. 2004; Roskosz et al. 2006, 2013; Watenphul et al. 2009, 2010; Yokochi et al. 2009; Kadik et al. 2011, 2013, 2015; Li et al. 2013, 2015, 2016b; Armstrong et al. 2015; Dalou et al. 2017a; Yoshioka et al. 2018), which has important consequences for planetary differentiation and subsequent evolution (e.g., Marty 2012; Johnson and Goldblatt 2015; Hirschmann 2016). This scientific advance raises the need to improve techniques for measuring N in geologic materials and to understand the mechanisms by which it is incorporated. Nitrogen can be difficult to quantify accurately—particularly at low concentration levels—with conventional, widely available microanalytical techniques such as electron probe microanalysis (EPMA) and secondary ion mass spectrometry (SIMS).

Measurement of nitrogen by EPMA has consistently been fraught with problems owing to its low fluorescence yield, resulting in low count rates and poor peak-to-background ratios (Bastin and Heijligers 1991; Raudsepp 1995). Furthermore, the curvature of the background on LDE monochromators as well as the presence of higher order metal interference lines can complicate analysis. Using a protocol that takes these factors into account, von der Handt and Dalou (2016; see also Dalou et al. 2017a and Supplementary[1] Material) achieved a detection limit of 0.04 wt% N in silicate glasses. This method represents a significant improvement over previous studies using EPMA. For instance, Roskosz et al. (2013) reported a practical detection limit of 0.15 wt% N. Li et al. (2015) achieved a lower detection limit (~0.05 wt% N) using a calibration curve technique, but this approach is limited to simple systems because it does not explicitly take matrix corrections into account (as is normally done with major and minor element EPMA data).

For most elements, SIMS offers lower detection limits than EPMA. In the case of N, however, analysis is impeded by low

* E-mail: jmosenfe@umn.edu

0003-004X/19/0001–031$05.00/DOI: https://doi.org/10.2138/am-2019-6533

useful ion yields of N^+ and negligible useful ion yields of N^- (useful ion yield is defined as the number of ions detected per atom or molecule of that species sputtered from the sample; e,g., Hervig et al. 2006). Accordingly, most SIMS analyses of N rely on measurement of CN^-/C^-, which is a well-established method for C-rich materials such as diamond and graphite (e.g., Fitzsimons et al. 1999), organic matter (Dekas et al. 2009; De Gregorio et al. 2011), and carbides and nitrides in meteorites (Zinner et al. 1989; Sugiura 1998).

Compared to these materials, less SIMS work has been performed on nitrogen in silicates. Carnera et al. (1990) reported concentrations of implanted N in fused silica, calculated from depth profiles of SiN^- sputtered with a Cs^+ primary beam. More recently, Williams et al. (2012, 2013), Li et al. (2013, 2015), Hervig et al. (2014), and Regier et al. (2016) pioneered new techniques for measuring N in silicate minerals and glasses. In the first study by Li et al. (2013), experimental samples were doped with ^{15}N during synthesis and matrix-matched reference materials were implanted with ^{15}N. Nitrogen concentrations were then quantified by measuring $^{15}N^{16}O^-/^{28}Si^-$ with a Cs^+ primary beam. Because separating the interference between $^{15}N^{16}O^-$ and $^{29}Si^1H_2^-$ requires a mass resolving power beyond the capability of the instrument that was used, a multi-step peak stripping procedure was employed to correct measured $^{15}N^{16}O^-/^{28}Si^-$ values. This correction resulted in an uncertainty of at least ±15%. Moreover, such an analytical protocol would be difficult to apply to samples with natural abundances of ^{15}N without using ion implantation. In their second study, Li et al. (2015) took a more straightforward approach by measuring $^{14}N^+/^{28}Si^{++}$ in silicate glasses using an O^- primary beam. This methodology was feasible despite the low ionization efficiency of $^{14}N^+$, because of the relatively high N concentrations in the samples that were studied. A similar approach was employed previously by Williams et al. (2012, 2013) and Hervig et al. (2014) to measure N in clays, cordierites, and silicate glasses. Similarly, Regier et al. (2016) measured natural and synthetic glasses using depth profiling of N-implanted samples for standardization and quantification based on $^{14}N^+/^{30}Si^+$. For selected samples, they also compared this methodology to depth profiling using NO^- and CN^- species.

In this study, we compare data acquired using SIMS to three other techniques: EPMA, FTIR, and laser-extraction mass spectrometry (Humbert et al. 2000). Building on previous work, we used different SIMS methods for quantifying N concentrations in experimentally synthesized N-rich silicate glasses and metals as well as one natural N-bearing silicate mineral, hyalophane. In the first approach, $^{14}N^+/^{30}Si^+$ was measured using an O^- primary beam. The same samples were then analyzed with a Cs^+ primary beam and $^{12}C^{14}N^-$ or $^{14}N^{16}O^-$ molecular ions were detected to quantify nitrogen contents using either $^{30}Si^-$ or $^{18}O^-$ as the reference mass. Metal alloys in equilibrium with some of the N-rich glasses were also measured using $^{14}N^+/^{54}Fe^+$ produced by an O^- primary beam. In this work, we discuss the advantages and disadvantages of these methods. For the silicate glasses in particular, we use our combined spectroscopic and chemical data in comparison to previous experimental work to place new constraints on N incorporation mechanisms, with attendant implications for N storage in planetary bodies.

METHODS

Sample description

Two types of basaltic glasses were studied: Fe-bearing and nominally Fe-free (hereafter referred to as "Fe-free" despite the presence of up to 0.05 wt% FeO, Table 1). Piston-cylinder synthesis of the Fe-bearing basaltic glasses is described in Dalou et al. (2017a). These glasses are in equilibrium with Fe-C-N metal alloys and were used to determine N and C partitioning between melt and metal as a function of P (between 1.2 and 3 GPa), T (1400 or 1600 °C), f_{O_2}, and composition. Some of the glasses are too Si-rich or Si-poor to classify sensu stricto as basalts, as a result of the differing amounts of Fe_4N or Fe added to the charge and the degree of metal alloy precipitation in the run product (Dalou et al. 2017a). The Fe-free basaltic glasses were also made at high P and T using a Fe-free MORB analog composition to which 0.3 to 9 wt% Si_3N_4 was added to vary the final N content (see Table 1). Starting materials were contained in graphite capsules (O.D. 4.5 mm, I.D. 3 mm, length 6–7 mm), which were inserted into CaF_2 pressure cells and run at 1.2 GPa and 1400 °C for 6 h (additional experimental details are given in Dalou et al. 2017a). Although the experiments were performed under nominally anhydrous conditions, significant amounts of hydrogen—bound structurally via multiple mechanisms—are incorporated in the run products as documented below.

The hyalophane (obtained from Andrew Locock at the University of Alberta, Canada) originates from the Zagradski Potok mine in Bosnia (Divljan 1954), the same locality studied by Beran et al. (1992).

TABLE 1. EPMA data for Fe-free glasses and hyalophane

Sample no.	B701	B702	B703	B704	B710	B711	Hyalophane
SiO_2	54.35(27)	54.21(38)	51.93(32)	52.61(11)	55.39(20)	58.55(25)	50.14(49)
TiO_2	0.89(7)	0.91(9)	0.96(7)	1.00(8)	0.85(8)	0.33(4)	n.a.
Al_2O_3	17.53(12)	17.14(11)	17.56(9)	17.19(14)	16.50(4)	16.46(10)	22.18(17)
MgO	10.00(7)	10.10(8)	10.22(6)	10.30(6)	10.03(13)	9.54(10)	b.d.l.
CaO	13.28(12)	13.36(12)	13.77(10)	13.48(8)	13.46(14)	12.67(5)	b.d.l.
BaO	n.a.	n.a.	n.a.	n.a.	n.a.	n.a.	19.60(6)
K_2O	0.11(1)	0.11(1)	0.10(1)	0.10(1)	0.10(1)	0.09(1)	6.90(13)
FeO	0.02(1)	b.d.l.	0.04(2)	0.05(3)	0.03(2)	0.05(1)	n.a.
SrO	n.a.	n.a.	n.a.	n.a.	n.a.	n.a.	0.35[a]
Na_2O	2.27(3)	2.25(3)	2.28(3)	2.23(3)	2.13(4)	2.09(5)	1.509 (3)
P_2O_5	0.03(1)	0.06(3)	0.07(2)	0.06(2)	0.05(2)	0.08(2)	n.a.
Cr_2O_3	0.09(3)	0.11(4)	0.10(3)	0.09(2)	0.09(1)	0.05(3)	n.a.
MnO	0.15(2)	0.15(1)	0.16(2)	0.16(1)	0.12(2)	0.14(3)	n.a.
N	0.360(24)	0.302(21)	0.083(11)	0.062(27)	0.767(32)	1.889(53)	0.113(15)
Total	99.09	98.72	97.27	97.33	99.52	101.92	100.79
No. analyses	10	10	10	10	10	10	7
Added Si_3N_4 [b]	1	2	0.5	0.3	5	9	n.a.

Notes: All values in weight percent. b.d.l. = below detection limit; n.a. = not analyzed or not applicable. Numbers in parentheses represent one standard deviation in terms of least units cited.

[a] Element not measured, value taken from Beran et al. (1992).

[b] Weight percent of Si_3N_4 added to Fe-Free MORB starting material.

EPMA

Major element and N compositional data for the Fe-bearing glasses and metal alloys are provided in Dalou et al. (2017a). Analyses of the Fe-free glasses and hyalophane are given in Table 1. All of these data were obtained using the methods outlined by von der Handt and Dalou (2016) and Dalou et al. (2017a). In brief, our methodology entails acquiring N data at 10 kV and 150 nA, separately from major element data at 15 kV and 20 nA. A 10 μm defocused beam is used in both cases. N*K*α peak intensities are aggregated from two LDE1 spectrometers, with special attention paid to setting background positions and fitting an exponential background (Donovan et al. 2011) on previously acquired wavelength scans. Examples of these scans are shown in the supplementary material[1]. In the case of hyalophane we increased count times from 80 s on peak and 120 s off peak to 300 s on peak and 300 s off peak, resulting in a detection limit of 0.01 wt% N. The data were blank-corrected using the algorithm outlined by Donovan et al. (2011) with three analyses each on forsterite (GRR1017) and Amelia albite, both presumed to be N-free, and the primary reference material for N was Si_3N_4. Final data processing employed the PROZA91 matrix correction (Bastin et al. 1998) and FFAST mass absorption corrections (Chantler et al. 2005).

Laser extraction static mass spectrometry

Nitrogen abundances and isotope ratios of the Fe-free glasses (Table 2) were determined by CO_2 laser extraction static mass spectrometry analysis at the Centre de Recherches Pétrographiques et Géochimiques (Humbert et al. 2000; Hashizume and Marty 2004). Small glass fragments were handpicked in an effort to avoid graphite inclusions. Fragments between 37 and 436 μg in mass were loaded into different pits of the laser chamber connected to the purification line of a Micromass VG5400 mass spectrometer. The sample chamber was pumped to ultra-high vacuum and kept at a temperature of 383 K overnight. The glass fragments were then heated individually to melting in a single heating step with a continuous-mode infrared CO_2 laser (λ = 10.6 μm). Several samples were reheated after being melted, demonstrating that ≥99.5% of the total nitrogen content was extracted during the first heating step. The extracted gas fraction was purified in a glass line using a CuO furnace cycled between 723 and 1073 K and a U-shaped cold trap held at 93 K. Prior to introduction into the mass spectrometer, the amount of molecular nitrogen was adjusted by volume dilution to match the amount of N_2 of an air standard, which was purified using the same procedure. Nitrogen isotope data were collected using a Faraday cup for masses 28 ($^{14}N^{14}N$) and 29 ($^{15}N^{14}N$), and an electron multiplier for masses 29 ($^{15}N^{14}N$) and 30 ($^{15}N^{15}N$) (see Hashizume and Marty 2004 for details). Procedural blanks (n = 5) averaged (9.6 ± 2.1) × 10^{-13} mol N_2 and are negligible compared to the amount of nitrogen contained in the samples. Isotope ratios of nitrogen ($^{15}N/^{14}N$) are expressed in delta (δ) notation, where ^{15}N (in ‰) = $[(^{15}N/^{14}N)_{sample}/(^{15}N/^{14}N)_{std} - 1] \times 1000$ and the standard is atmospheric N_2 with $^{15}N/^{14}N = 0.003676$. All nitrogen data have been corrected for blank contributions, CO and C_2H_x interferences, and instrumental mass fractionation. The reported uncertainties (1*s*) include both external uncertainties (repeat analyses of the air standard) and internal uncertainties (counting statistics) but largely depend on the reproducibility of air standard nitrogen abundance (1.1%) and isotope ratio (0.25%) measurements (n = 14).

TABLE 2. Laser extraction mass spectrometry results for Fe-free glasses

Sample	Chip ID	Weight (mg)	N_2 mol	N μg/g	$\delta^{15}N$ (‰)	1*s*
701	701-2	256	3.15E-08	3449(37)	−8.9	2.5
701	702-3	37	4.12E-09	3120(33)	−7.3	3.0
average (1*s*)				**3284(233)**		
702	702-1	98	7.09E-09	2025(22)	−7.7	2.6
702	702-2	436	3.78E-08	2430(26)	−9.5	2.5
average (1*s*)				**2228(286)**		
703	703-1	95	2.63E-09	776(8)	−5.4	3.2
703	703-2	182	4.21E-09	648(7)	−3.0	2.5
	703-2re		*1.95E-11*	*3*	*23.2*	*10.1*
703	703-3	51	1.31E-09	720(8)	−9.9	2.5
average (1*s*)				**714(64)**		
704	704-1	176	2.56E-09	407(4)	−3.1	2.5
	704-1re		*1.11E-11*	*2*	*−0.3*	*22.0*
704	704-2	212	2.72E-09	360(4)	−0.7	2.5
average (1*s*)				**383(33)**		
710	710-1	158	3.67E-08	6505(69)	−9.0	2.5
	710-1re		*1.83E-10*	*32*	*−17.2*	*7.8*
710	710-2	145	3.80E-08	7334(78)	−9.7	2.5
710	710-3	292	7.10E-08	6812(73)	−3.9	3.0
	710-3re		*4.13E-10*	*40*	*−8.6*	*2.6*
average (1*s*)				**6883(419)**		
711	711-1	65	4.36E-08	18872(200)	−6.3	2.5
711	711-2	225	1.54229E-07	19193(205)	−6.6	2.5
711	711-3	245	1.5184E-07	17353(185)	−8.6	2.6
	711-3re		*3.38862E-10*	*39*	*−10.0*	*6.1*
average (1*s*)				**18443(966)**		

Notes: Values in italics are for samples that were reheated after melting. Numbers in parentheses are 1*s* uncertainties in terms of least units cited. Uncertainties for $\delta^{15}N$ are given in a separate column. Averages are only for results from initial heating steps.

FTIR

Doubly polished chips of the Fe-free glasses were used to acquire FTIR spectra with a Bruker Tensor 37 spectrometer attached to a Hyperion 2000 microscope, using methods outlined in Armstrong et al. (2015). The chips were measured at different thicknesses (with progressive thinning) to obtain spectra with low signal-to-noise ratios and peak absorbances less than 2 in both the near-infrared (NIR) and mid-infrared (MIR) regions.

An inclusion-free chip cut from the same single crystal of hyalophane used for EPMA and SIMS was prepared for FTIR in the form of a cuboid that was oriented optically to obtain polarized spectra in the α, β, and γ directions. The path lengths of the measurements were either 0.49 or 0.86 mm, and the estimated uncertainty in optic orientations is ±2°. A CaF_2 wire-grid polarizer was used for these measurements, which were also taken in the microscope. Data below 2000 cm^{-1} were acquired on two thinner chips cut from a separate single crystal, allowing us to obtain complementary polarized spectra in the α, β and γ directions albeit with higher uncertainty in orientation (estimated to be ±5°).

SIMS

Sample chips were polished, cleaned, dried, and mounted in a single indium mount for SIMS analysis using well-established methods for low-blank analysis (Aubaud et al. 2007). The mount was gold coated for SIMS analysis after baking overnight in a vacuum oven at 100 °C.

The majority of our SIMS measurements were performed on the Cameca 6f at Arizona State University (ASU) over a five-day period. Three additional analyses of hyalophane were acquired using the Cameca 7f-GEO at Caltech, using a Cs^+ primary beam and previously outlined techniques (Mosenfelder et al. 2015), to acquire additional H and F data. For the analyses at ASU, an O^- primary ion beam was used for the first three days, after which the source was changed to a Cs^+ beam. The immersion lens in the secondary optic column was cleaned just prior to the session, and the instrument was not baked, resulting in higher vacuum (~6 to 7 × 10^{-7} Pa) compared to typical sessions using epoxy-free samples mounted in indium (typically ~2 to 5 × 10^{-8} Pa). However, all of our samples yielded counts for $^{14}N^+$ (with the O^- beam), $^{14}N^{16}O^-$, and $^{16}OH^-$ (with the Cs^+ beam) well above background levels periodically measured on GRR1017 forsterite, presumed to be N- and H-free (Mosenfelder et al. 2011).

The O^- beam analyses were acquired using a beam current of ~20 nA with an impact energy of 21.5 keV, with the beam tuned manually for each analysis in critical illumination mode prior to manual mass calibration. Positive secondary ions were accelerated to 9 kV, the energy bandpass was set to allow ions with ~0 ± 20 eV into the mass spectrometer, and sample charging was controlled by scanning the sample voltage (while monitoring $^{30}Si^+$) and returning the sample voltage to the centroid of the $^{30}Si^+$ vs. sample voltage curve (e.g., Hervig et al. 2003). Surface contamination was mitigated by pre-sputtering for 10 minutes, with the beam rastered to produce craters approximately 120 × 90 μm in size. A manually centered field aperture was used to collect ions restricted to the central 15 μm of each crater. In some cases, secondary ion images of ^{54}Fe were obtained prior to insertion of the field aperture to preclude analysis of Fe-N-C melt spheres in the Fe-rich glasses, which were much smaller than the size of the SIMS crater for some samples (Dalou et al. 2017a). We also analyzed the quenched Fe-N-C melts in samples that contained spheres large enough to analyze without contamination by the surrounding glass. Each glass analysis comprised 15 cycles through the mass sequence $^{12}C^+$ (3*s*), $^{14}N^+$ (9*s*), and $^{30}Si^+$ (1*s*), and secondary ions were collected by an electron multiplier with counts corrected for detector background and counting system dead time. ^{54}Fe (1*s*) was added to the mass sequence for Fe-N-C alloys, and the data were blank-corrected using measurements on a pure Fe metal reference material. As shown in Figure 1a, a mass resolution of ~1350 (M/ΔM) was used to separate $^{12}C^+$ from $^{24}Mg^{++}$ and $^{14}N^+$ from $^{28}Si^{++}$ and $^{12}CH_2^+$; on the second day of the session the mass resolution was reduced to ~1250 to increase counts while still resolving the $^{14}N^+$ peak, at the

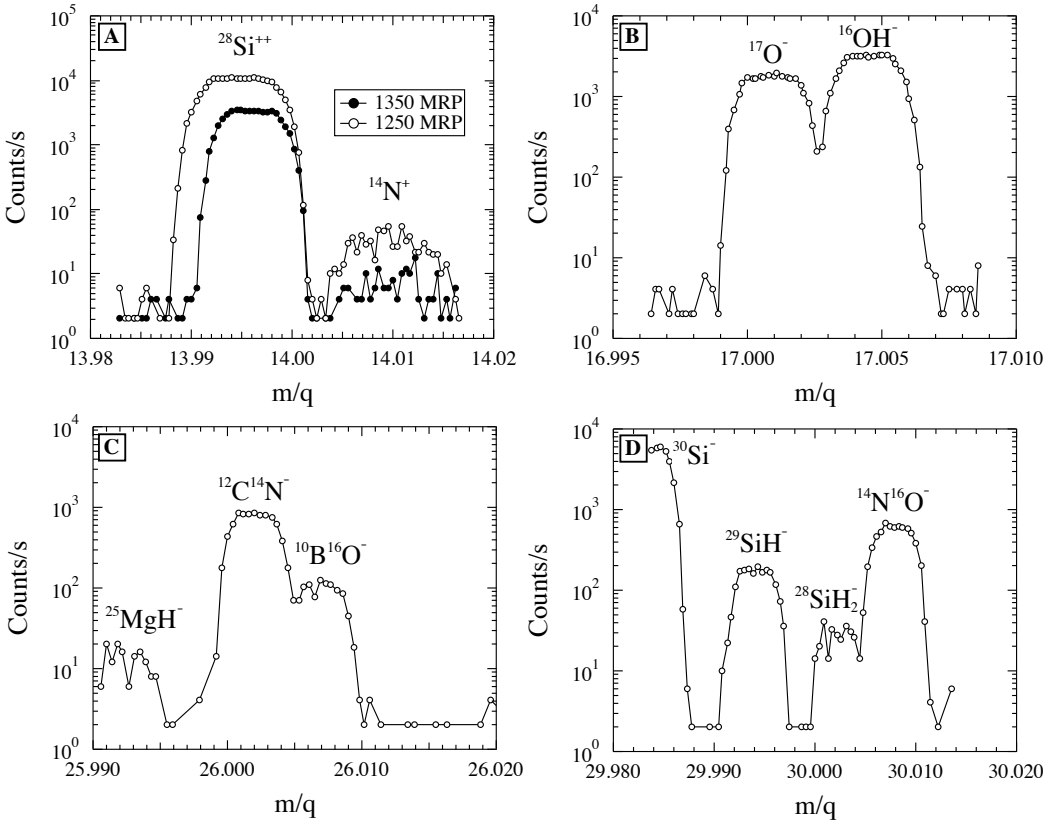

Figure 1. High-resolution mass scans, showing separation of peaks for species as labeled. (**a**) Scans on sample B703 using O^- primary beam, at mass resolving powers (MRP) of ~1350 (filled circles) and ~1250 (open circles). (**b**–**d**) Scans on sample B710 using Cs^+ primary beam at MRP of ~5000.

cost of full separation of $^{12}C^+$ from $^{24}Mg^{++}$ (not shown in Fig. 1).

For Cs^+ beam analyses we used a beam current of 8 to 10 nA with an impact energy of 15 keV, with secondary ions accelerated to –5 kV. Charge compensation was achieved with a normal incidence electron flood gun, tuned using the method of Chen et al. (2013). Pre-sputtering duration after primary beam tuning and mass calibration was three minutes. The beam was rastered to produce square craters ~40 μm in diameter, with a field aperture used to collect ions restricted to the central 8 μm. Metal alloy precipitates were avoided using ion images of ^{12}C. Twenty cycles were collected for each analysis through the mass sequence $^{12}C^-$ (5*s*), $^{16}OH^-$ (2*s*), $^{18}O^-$ (1*s*), $^{12}C^{14}N^-$ (2*s*), $^{30}Si^-$ (1*s*), and $^{14}N^{16}O^-$ (2*s*). The mass resolution was set to ~5000 to resolve $^{16}OH^-$ from $^{17}O^-$ (Fig. 1b), $^{12}C^{14}N^-$ from $^{25}MgH^-$ and $^{10}B^{16}O^-$ (Fig. 1c), and $^{14}N^{16}O^-$ from $^{30}Si^-$, $^{29}SiH^-$, and $^{28}SiH_2^-$ (Fig. 1d). $^{10}B^{16}O^-$ arises from surface contamination. This resolving power is not sufficient to separate $^{12}C^{14}N^-$ from $^{13}C_2^-$, which is important for analysis of N in diamonds (Fitzsimons et al. 1999) but irrelevant for this study given the trace concentrations of carbon in our samples and low secondary ion yield of this dimer (Burdo and Morrison 1971). $^{12}C^{18}O^-$ is resolved from $^{30}Si^-$ at this resolution but was not observed in high mass resolution scans.

Carbon and H_2O concentrations in the glasses (Table 3) were determined from $^{12}C/^{18}O$ and $^{16}OH/^{18}O$, respectively, blank-corrected using GRR1017 forsterite. Carbon and H_2O reference materials as well as GRR1017 were measured multiple times during the two days of Cs^+ beam analysis. For C, we used four synthetic basaltic glasses with CO_2 contents ranging from 0.52 to 2.01 wt% (B248, B274, B291, and B311; Stanley et al. 2011), and ALV519-4-1, a natural basaltic glass with a well-established CO_2 content of 165 μg/g (Fine and Stolper 1985). Four basaltic glasses (ALV519-4-1, JdFD10, KN54Sta51, and KN54Sta52; Aubaud et al. 2007) with H_2O contents ranging from 0.17 to 0.65 wt% were used for the H_2O calibration. York regressions (York 1966) were applied to calibration data collected on the two separate days. Assessed in this manner, we observed drifts in the H_2O and CO_2 calibrations of ~18 and 3%, respectively. Furthermore, some previous calibrations for glasses have shown statistically significant curvature at water contents above 1–2 wt% (Hauri et al. 2002; Hervig et al. 2003; Aubaud et al. 2007; Tenner et al. 2009; Mosenfelder, unpublished data). Therefore, our linear fits may result in underestimation of total H_2O for samples with contents exceeding the range in the standards. Given these uncertainties, we emphasize that the exceptionally low uncertainties cited in Table 3 for some samples reflect only the standard deviation (2*s*) of the measurements, not their accuracy.

SIMS craters were examined after the session at ASU using secondary electron (SE) imaging and EDS mapping on the microprobe to assess whether contamination from cracks or inadvertent overlap between phases influenced the data. We also used excessive ^{12}C counts relative to other analyses on a given sample and/or the Poisson counting statistic criterion of Mosenfelder et al. (2011) to exclude some analyses from the final averages provided in Table 3. For two analyses (for B701 and B711, see Table 3), we rejected the ^{12}C counts for the sake of C measurement (owing to apparent surface contamination), yet $^{12}C^{14}N^-$ data were in line with replicate analyses. In the case of Fe-N-C alloys (Table 4), we excluded some analyses with abnormally low ^{54}Fe and high ^{30}Si cps, reflecting probable contamination from silicate glass.

Results

Fe-free glasses

Six Fe-free glasses with different N contents were measured by EPMA (Table 1), laser extraction mass spectrometry (Table 2), and FTIR (Supplemental[1] Table S1); five of these glasses were analyzed by SIMS. SIMS data are summarized in Table 3, and the primary data (individual analyses, including uncertainties expressed as the standard error of the mean, $2s_{\bar{x}}$, as well as Poisson counting statistics) are provided in the supplementary[1] material.

Nitrogen contents range from 0.04 to 1.84 wt% as measured

TABLE 3. SIMS data for silicate glasses and hyalophane

Sample no.	No. analyses [a]	N wt% EPMA	H_2O (wt%) SIMS [b]	H/N	SiO_2 wt% EPMA	$^{14}N^+/^{30}Si^+$	$^{12}C^-/^{18}O^-$	C (ppmw)	$^{16}O^1H^-/^{18}O^-$	$^{12}C^{14}N^-/^{18}O^-$	$^{12}C^{14}N^-/^{30}Si^-$	$^{14}N^{16}O^-/^{18}O^-$	$^{14}N^{16}O^-/^{30}Si^-$
Fe-free glasses													
B701	3/3	0.360(48)	0.553(2)	2.39	54.4	0.000274(13)	0.00986(8)	51.5(4)	1.302(5)	0.0346(38)	0.0861(64)	0.020(5)	0.048(5)[c]
B703	6/6	0.083(22)	1.08(4)	20.23	51.9	0.000091(10)	0.00530(46)	28(2)	2.542(90)	0.0071(19)	0.0168(35)	0.007(3)	0.016(3)
B704	3/3	0.062(54)	1.47(3)	36.89	52.6	0.000065(8)	0.00608(25)	32(1)	3.463(74)	0.0072(8)	0.0166(4)	0.006(1)	0.014(2)
B710	6/3	0.767(64)	0.604(8)	1.22	55.4	0.000438(19)	0.01381(5)	72.1(3)	1.421(18)	0.0912(66)	0.189(15)	0.048(14)	0.100(15)
B711	3/3	1.889(106)	0.67(4)	0.55	58.5	0.000598(62)	0.0224(83)	117(43)	1.570(91)	0.195(40)	0.430(25)	0.085(25)	0.187(28)[c]
Fe-bearing glasses													
B697	2/3	0.117(23)	0.34(1)	2.98	58.0	0.000171(10)	0.0094(10)	49(5)	0.81(3)	0.0159(13)	0.030(7)	0.015(7)	0.027(5)
B706a	3/3	0.089(28)	0.68(2)	11.86	51.4	0.000087(11)	0.0149(4)	78(2)	1.60(4)	0.0113(17)	0.025(3)	0.008(3)	0.016(3)
B706b	3/3	0.090(27)	0.500(8)	8.61	52.4	0.000102(9)	0.0135(5)	70(3)	1.18(2)	0.0120(10)	0.025(1)	0.008(2)	0.017(3)
B706c	3/3	0.042(14)	1.04(1)	38.07	44.4	0.000032(3)	0.0210(5)	110(2)	2.46(2)	0.0076(4)	0.018(2)	0.004(1)	0.011(1)
B707b	3/3	0.132(43)	1.3(2)	15.35	44.6	0.000072(12)	0.0261(42)	141(23)	2.47(38)	0.0088(19)	0.024(6)	0.007(3)	0.020(4)
B707c	3/3	0.225(23)	0.86(4)	5.94	51.0	0.000177(21)	0.0186(71)	101(38)	1.66(8)	0.0118(29)	0.029(6)	0.012(2)	0.029(4)
B712a	3/2	0.138(27)	0.716(1)	8.08	42.8	0.000074(7)	0.0933(5)	487(3)	1.684(2)	0.900(3)	0.196(16)	0.015(2)	0.032(1)
B712b	3/2	4.761(67)	0.191(4)	0.06	58.1	0.001028(12)	0.0769(26)	401(13)	0.450(9)	1.04(15)	1.75(18)	0.211(84)	0.351(53)
B712c	1/0	0.119(38)	–	–	47.1	0.000115(3)	–	–	–	–	–	–	–
B712d	3/3	0.781(27)	0.289(8)	0.58	58.8	0.000541(18)	0.0373(9)	195(4)	0.68(2)	0.206(24)	0.392(71)	0.052(22)	0.098(15)
B712e	3/3	0.263(12)	0.49(3)	2.89	52.1	0.000187(8)	0.0494(18)	258(9)	1.16(7)	0.095(6)	0.190(21)	0.022(6)	0.045(4)
B712f	3/3	0.142(40)	0.72(1)	7.90	45.0	0.000071(22)	0.063(27)	328(142)	1.70(3)	0.062(36)	0.127(71)	0.015(4)	0.031(7)
B714a	2/0	0.172(36)	–	–	43.6	0.000108(3)	–	–	–	–	–	–	–
B714b	3/3	0.429(19)	0.493(5)	1.79	51.7	0.000232(59)	0.0442(25)	239(13)	0.95(1)	0.058(6)	0.126(9)	0.024(2)	0.053(2)
B714d	3/3	0.376(33)	0.59(4)	2.44	50.6	0.000223(22)	0.041(14)	223(76)	1.14(7)	0.049(37)	0.118(73)	0.018(8)	0.044(14)
B714e	3/3	5.418(19)	0.36(1)	0.10	64.3	0.001584(75)	0.050(12)	263(64)	0.85(3)	0.63(13)	0.920(99)	0.225(96)	0.327(65)
B727a	4/3	0.343(30)	0.415(6)	1.88	45.5	0.000313(64)	0.0405(18)	212(9)	0.98(1)	0.131(5)	0.240(12)	0.032(5)	0.058(4)
B727b	3/3	0.214(42)	0.75(3)	5.44	43.6	0.000175(21)	0.0500(61)	270(33)	1.45(5)	0.041(7)	0.093(15)	0.014(1)	0.031(2)
B727c	2/2	0.164(52)	0.604(6)	5.73	46.5	0.000156(17)	0.0355(17)	192(9)	1.16(1)	0.035(20)	0.071(27)	0.014(6)	0.028(7)
B727d	3/3	0.191(35)	1.02(3)	8.33	46.9	0.000122(31)	0.039(31)	213(167)	1.96(6)	0.028(29)	0.061(62)	0.011(5)	0.024(8)
B727e	3/3	0.239(19)	0.57(3)	3.71	49.0	0.000197(18)	0.0500(48)	270(26)	1.09(5)	0.041(16)	0.095(29)	0.012(4)	0.029(6)
B727f	3/3	0.257(17)	0.33(2)	2.00	45.5	0.000212(33)	0.0425(64)	222(33)	0.77(6)	0.105(16)	0.185(24)	0.025(9)	0.044(4)
Hyalophane	2/3	0.113(30)	*see text* [d]	*see text* [d]	50.1	0.000056(8)	bdl	–	0.099(6)	bdl	bdl	0.0010(2)	0.0026(2)

Notes: Uncertainties (in parentheses) are 2*s* of multiple analyses or $2s_{\bar{x}}$ in case of a single analyis. All SIMS data blank corrected using GRR1017 forsterite.
[a] Numbers before and after slash are O^- and Cs^+ primary beam analyses, respectively.
[b] Total H_2O content calculated from $^{16}O^1H/^{18}O$, inferred to include contributions from O-H, N-H, C-H, and H_2 species.
[c] ^{12}C data (only) were rejected for one out of three analyses in the case of these two samples, owing to surface contamination.
[d] Total H_2O ($NH_4 + H_2O + OH$) content determined by multiple methods, see text for explanation.

TABLE 4. SIMS data for metals

Sample no.	No. analyses	N wt% EPMA	$^{14}N/^{54}Fe$
B706a	2	1.05(3)	0.00038(11)
B706b	1	1.08(1)	0.00043(1)
B706c	2	0.99(2)	0.00043(6)
B707c	1	1.82(8)	0.00101(1)
B712a	1	1.86(13)	0.00088(1)
B712b	2	1.54(21)	0.00057(2)
B712f	1	1.93(6)	0.00083(1)
B727b	2	1.98(6)	0.00113(27)
B727c	1	1.96(5)	0.00106(1)
B727e	2	1.96(4)	0.00084(3)

Notes: Uncertainties (in parentheses) are 2*s* of multiple analyses or $2s_{\bar{x}}$ in case of a single analysis. All SIMS data blank corrected using Fe metal.

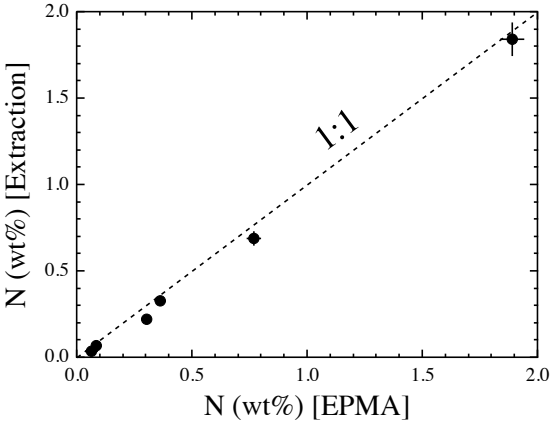

FIGURE 2. N concentrations in Fe-free glasses as determined by laser extraction mass spectrometry vs. EPMA, with error bars (2*s*) shown. Dashed line shows 1:1 correspondence.

by extraction and 0.06 to 1.89 wt% as measured by EPMA. $\delta^{15}N$ ranges from –9.9 to 0.7‰; we ascribe no particular meaning to these values because the glasses were not in equilibrium with metallic alloys, in contrast to the study of Li et al. (2016b). Concentrations measured by EPMA are consistently higher than those determined by extraction (Fig. 2) but agree within mutual 2*s* uncertainties, demonstrating the general veracity of the EPMA method. Reproducibility (for two to three measurements per sample) ranges from 5 to 13% (1*s*) for the extraction method, with the lowest precision (9 to 13%) achieved for the lowest concentration samples (B702, B703, and B704). The reproducibility of the EPMA measurements (for 10 measurements per sample) follows a similar pattern, ranging from 3 to 7% for the three highest N-concentration samples and from 7 to 44% for the lowest concentration samples. The suitability of the Fe-free glasses as reference materials for N analysis is discussed in the Supplementary[1] Material.

FTIR spectra reveal complex speciation behavior for N and H in the Fe-free glasses, including structurally bound N-H, O-H, H_2O, and H_2, similar to previously published spectra of silicate glasses containing N (Kadik et al. 2013, 2015; Armstrong et al. 2015). For the sake of clarity, we show separate graphs for three different frequency regions: the NIR between 4000 and

5400 cm^{-1}, which reveals the presence of H_2 (with a band at 4107 cm^{-1}) as well as combination bands resulting from bending and stretching of H_2O, O-H and N-H complexes (Fig. 3a); the MIR between 2000 and 4000 cm^{-1}, where O-H and N-H fundamental stretching vibrations occur (Fig. 3b); and the low wavenumber MIR from 1300 to 2000 cm^{-1}, dominated in these samples by bending modes of H_2O and N-H molecules (Fig. 3c). We also show an enlargement of the N-H stretching region for selected samples in Figure 3d. Overall, the spectra show an evolution with increasing N content from glasses containing mostly H_2O + OH (characterized by an O-H stretching band at ~3550 cm^{-1}, the bending mode for H_2O at 1635 cm^{-1}, and combination bending and stretching vibrations at 5200 and 4500 cm^{-1}) to glasses dominated by N-H complexes and H_2. The subtleties of N-H incorporation mechanisms are explored further in the discussion section, where we also consider the fact—based on mass balance considerations—that other N-species (N^{3-}, CN^-, and/or molecular N_2) *not* associated with H must also be important for N incorporation in these glasses.

We see no evidence in any of the samples for structurally bound CO_3^{2-} (characterized by a doublet at 1430 and 1520 cm^{-1}), CO_2 (showing a single peak near 2350 cm^{-1}), C≡O (characterized by bands in the region between ~2100 and 2200 cm^{-1}; Armstrong et al. 2015), or C≡N (with strong stretching vibrations typically between 2220 and 2260 cm^{-1}; Smith 1999). On the other hand, trace amounts of CH_4 or CH_3^- could be present; these species are difficult to detect in glasses with FTIR and more readily studied by Raman spectroscopy (Ardia et al. 2013).

Carbon concentrations determined by SIMS range from 28 to 117 μg/g (Table 3). Overall, the low C concentrations in these graphite-saturated experiments are consistent with Fe-bearing basalts previously synthesized at low f_{O_2}, below the iron-wüstite (IW) buffer (Armstrong et al. 2015; Dalou et al. 2017a). However, the positive correlation of C and N concentrations (Fig. 4a)

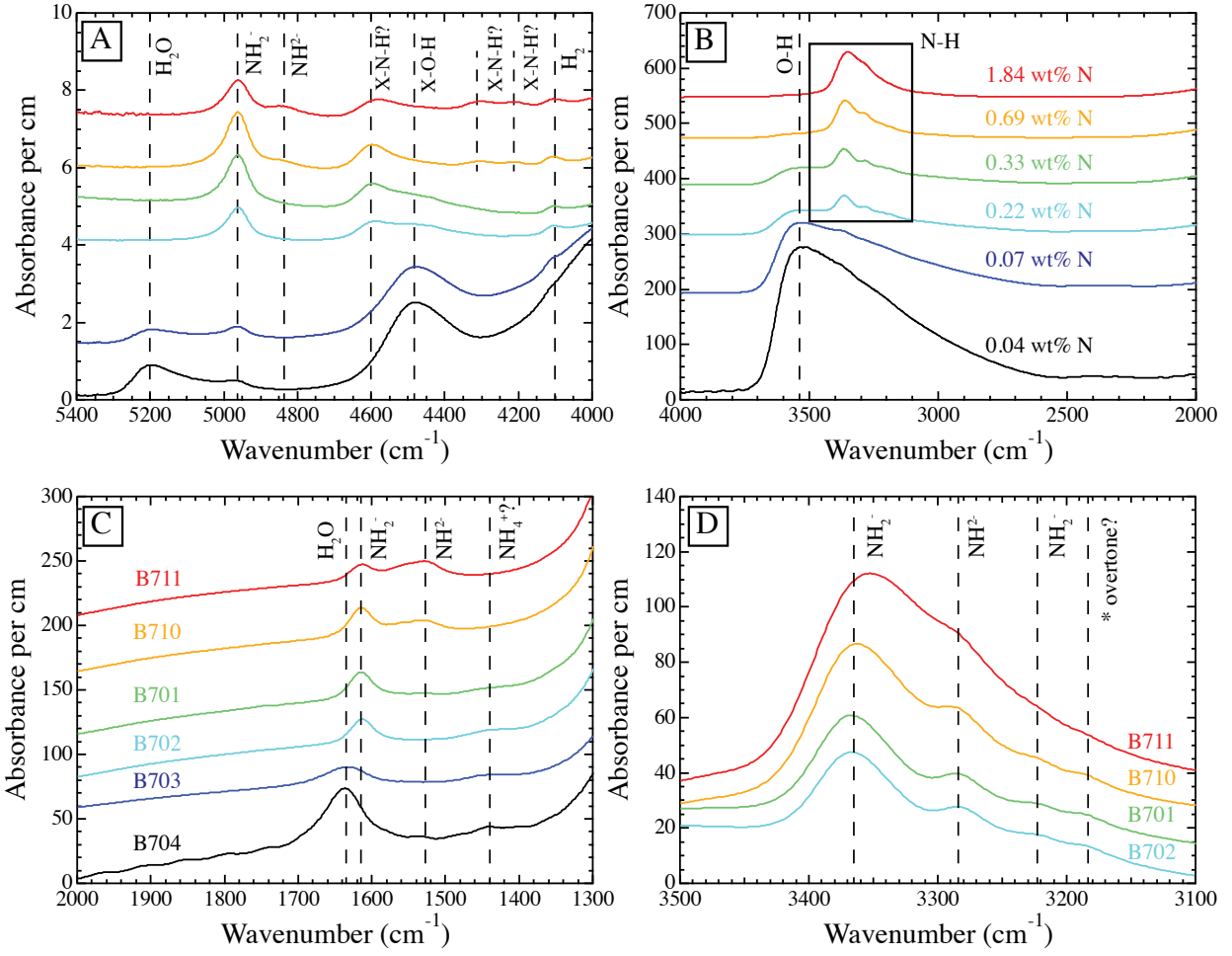

Figure 3. FTIR spectra of quenched Fe-free basaltic glasses. All spectra are normalized to 1 cm thickness, shown without baseline correction, offset for clarity, and stacked in order of total N content (low to high, bottom to top). (**a**) Near-infrared region, showing combination (stretching plus bending) bands for H_2O, O-H, and N-H species, as well as vibrational mode for H_2. (**b**) Mid-infrared spectra showing fundamental N-H and O-H stretching vibrational bands. The box outlines the region enlarged in **d**. Nitrogen contents as determined by extraction are labeled above each corresponding spectrum. (**c**) Mid-infrared spectra showing bending modes for H_2O and N-H species. Experiment numbers are labeled above each corresponding spectrum. (**d**) Detail of spectra in the N-H stretching region for the four most N-rich samples. Peak assignments are discussed in the text. "*overtone?" refers to speculative assignment to an overtone of the peak at 1615 cm^{-1} assigned to NH_2 bending, as labeled in **c**. (Color online.)

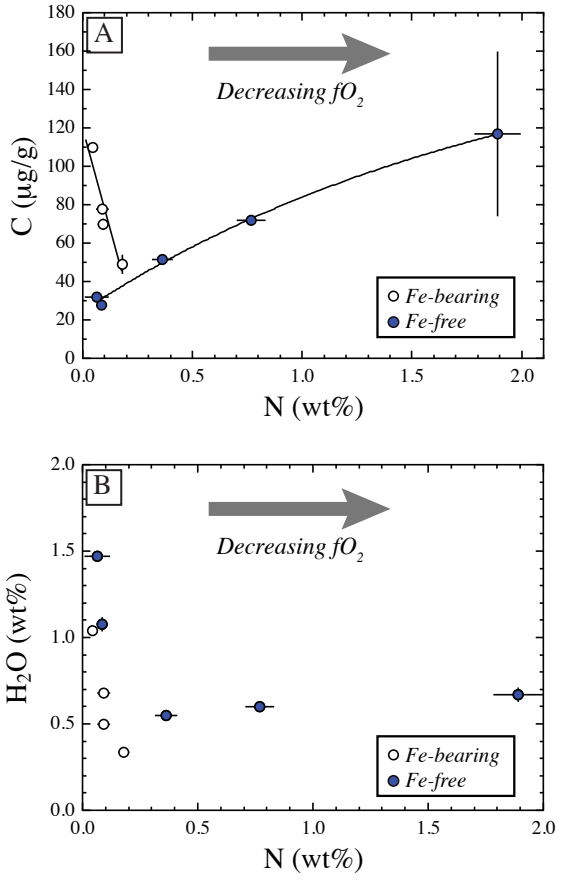

FIGURE 4. C (**a**) and H (**b**) concentrations (expressed as total H_2O content) as a function of N content in Fe-free (filled circles) and Fe-bearing glasses (open circles) at 1.2 GPa and 1400 °C. Curve fits shown in **a** are exponential and linear functions for Fe-free data and Fe-bearing data, respectively. The trend of decreasing f_{O_2} shown with the arrow in **a** is based on calculations for the Fe-bearing samples (Dalou et al. 2017a) and inference based on starting composition for the Fe-free samples. (Color online.)

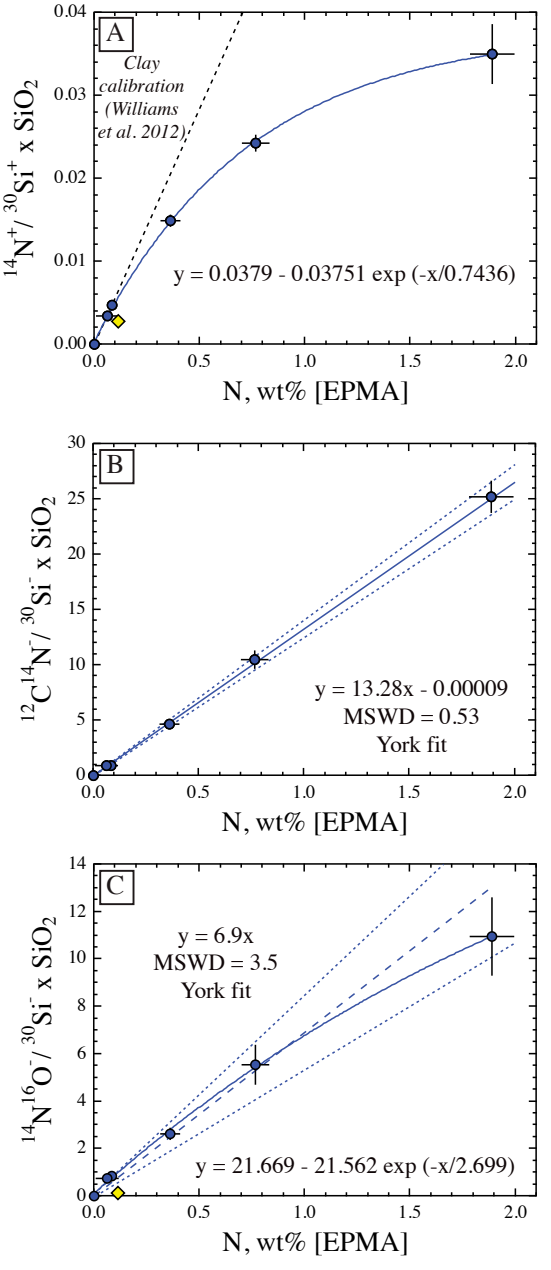

FIGURE 5. SIMS data for Fe-free glasses (circles) and hyalophane (diamond), plotted against N contents determined by EPMA. Ratios are normalized for SiO_2 content determined by EPMA. Error bars (2*s*) not shown are within symbol size. The point at the origin in each graph represents GRR1017 forsterite, used for blank correction. (**a**) $^{14}N^+/^{30}Si^+$ data. Solid curve is an exponential fit to the glass data with equation shown. Dashed line is the calibration for N-bearing clays from Williams et al. (2012), blank corrected by subtracting the intercept from their equation. (**b**) $^{12}C^{14}N^-/^{30}Si^-$ data. Hyalophane is not plotted because $^{12}C^{14}N^-$ counts were below the detection limit. The solid line is a York fit with the equation shown; dotted lines denote 95% confidence interval. Ordinary least squares (OLS) regression (not shown) yields an excellent fit (r^2 = 1, $p < 0.001$). (**c**) $^{14}N^{16}O^-/^{30}Si^-$ data. The solid curve is an exponential fit to the glass data with the equation shown. The dashed line is a York fit to the same data with the equation shown; dotted lines denote 95% confidence interval. (Color online.)

is inconsistent with the trend for Fe-bearing basalts synthesized by Dalou et al. (2017a) at the same *P-T* conditions (1.2 GPa and 1400 °C) but at varying f_{O_2}. Note that whereas f_{O_2} was calculated in the latter experiments based on the Fe and FeO concentrations of coexisting alloy and silicate melt, respectively, the schematic trend of decreasing f_{O_2} for the Fe-free glasses shown in Figure 4a is inferred based on amounts of added Si_3N_4, which is a reducing agent.

As shown in Figure 4b, total H_2O contents measured by SIMS initially decrease steeply with increasing N content for both Fe-free and Fe-bearing glasses synthesized at the same *P-T* conditions; between 0.36 and 1.89 wt% N, H_2O in the Fe-free samples increases slightly, by 0.12 wt%. The yield of $^{16}O^1H^-$ ions must reflect contributions via recombination from multiple structurally bound species in the glasses (including N-H and H_2) because some samples (B710 and B711) in fact contain little or no O-H or H_2O (Fig. 3).

SIMS results for N are shown in Figure 5 as three separate graphs for different isotopic ratios: $^{14}N^+/^{30}Si^+$ (Fig. 5a),

$^{12}C^{14}N^-/^{30}Si^-$ (Fig. 5b), and $^{14}N^{16}O^-/^{30}Si^-$ (Fig. 5c). Each data point represents an average of three to six analyses (Table 3). The ratios in Figure 5 are multiplied by SiO_2 content, which ranges from 52 to 59 wt%, but the trends and quality of curve fitting to the three data sets are essentially identical in each case if the data are not normalized in this fashion. Likewise, the same trends are observed if $^{18}O^-$ is used as the reference mass for the y-axis, or the concentrations determined by laser extraction are assumed for the x-axis.

The $^{14}N^+/^{30}Si^+$ data are best fit by an exponential function (Fig. 5a), although the data up to 0.1 wt% N can be fit to a linear function that agrees with the calibration for N in clays published by Williams et al. (2012). In contrast, the $^{12}C^{14}N^-/^{30}Si^-$ data are exceptionally well fit to linear functions throughout the range of N concentrations. We show a York regression in Figure 5b; an ordinary least squares (OLS) regression not taking uncertainties into account yields a correlation coefficient (r^2) of 1 ($p < 0.001$). The $^{14}N^{16}O^-/^{30}Si^-$ data can also be reasonably fit to a line up to 0.8 wt% N, but an exponential function better fits all of the data, as shown by the solid curve in Figure 5c. Note that polynomial functions can also be fit (albeit less precisely) to the $^{14}N^+/^{30}Si^+$ and $^{14}N^{16}O^-/^{30}Si^-$ data sets and we do not ascribe any particular physical or chemical meaning to the derived exponential functions.

Useful ion yields cannot be calculated from our data because crater dimensions were not measured after the SIMS session (cf. Hervig et al. 2006; Regier et al. 2016). Furthermore, count rate comparisons are complicated by the fact that machine parameters varied considerably between the Cs^+ and O^- beam analyses. Count rates varied even among the O^- beam analyses, considering that MRP was reduced on the second day of the session—which resulted in a factor of ~2 increase in ion yield but no discernible shift in relative sensitivity factor (RSF). Nevertheless, a rough comparison of counting rates (normalized to primary beam current) is useful for evaluating the efficiency of the O^- beam vs. Cs^+ beam methods. Taking B701 (with 0.36 wt% N) as an example, average counting rates were 2.9 cps/nA of $^{14}N^+$ (at MRP = 1350; 5.5 cps/nA at MRP = 1250); 69 cps/nA of $^{12}C^{14}N^-$; and 39 cps/nA of $^{14}N^{16}O^-$.

Fe-bearing glasses

SIMS data (Table 3) were acquired on 23 of the Fe-bearing glasses from the study of Dalou et al. (2017a). Based on EPMA, Dalou et al. showed that N increases dramatically in these glasses with decreasing f_{O_2}. Figure 6 shows that H (measured in all but two of the glasses) decreases with increasing N content (and thus decreasing f_{O_2}). The trends in Figure 6 show a monotonic decrease in H content with increasing N content at all *P*-*T* conditions, except for the series conducted on a MORB composition at 3 GPa and 1600 °C. Scatter in those data could reflect the relatively tight range in f_{O_2} conditions (from ΔIW-1.1 to ΔIW-1.84) covered by the six individual glasses from experiment B727.

SIMS data directly relevant to N are shown for three different ion ratios: $^{14}N^+/^{30}Si^+$ (Fig. 7a), $^{12}C^{14}N^-/^{30}Si^-$ (Fig. 7b), and $^{14}N^{16}O^-/^{30}Si^-$ (Fig. 7c). All of the data were normalized for SiO_2 content, which varied more (from 43 to 64 wt%) in these glasses compared to the Fe-free samples. The graphs also differ from those in Figure 5 because we show individual analyses rather than plotting averages with 2*s* error bars (which have

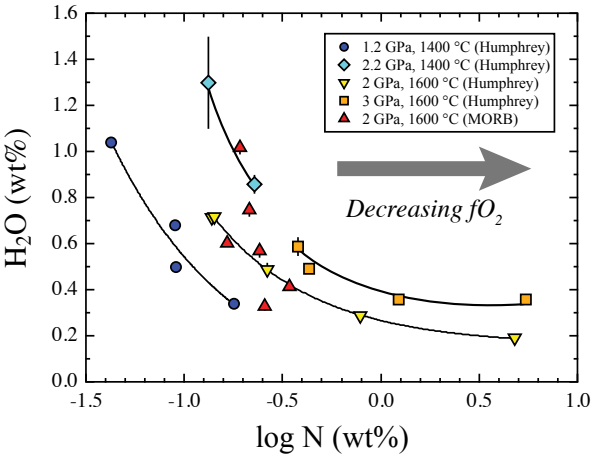

FIGURE 6. H concentration in Fe-bearing glasses as a function of N content. Schematic trend lines are shown for all data series at constant *P* and *T* except for the data on the MORB composition at 3 GPa and 1600 °C (experiment B727), which show a higher degree of scatter than the other data sets. The trend of decreasing f_{O_2} is based on calculations from Dalou et al. (2017a). (Color online.)

little meaning in the case of samples with only two analyses). Overall, the SIMS plots for the Fe-bearing glasses show more scatter than the graphs for the Fe-free samples, and the data extend to much higher N concentrations. The $^{14}N^+/^{30}Si^+$ data (Fig. 7a) are again best fit with an exponential function, which is nearly coincident up to 1 wt% N with the regression applied to the Fe-free glass data (shown by the dotted line for comparison). The two samples with the highest N concentrations are difficult to fit together, and reasons for their deviation from the best-fit line are unclear. Contamination of analyses by Fe-N-C alloys is a consideration. However, in the case of B712b (4.76 wt% N), alloy spheres were clustered around the edges of the glass and should have been avoided. B714e, with 5.42 wt% N, contains smaller alloy spheres distributed throughout the glass. Despite the use of ion imaging during SIMS and examination by SEM of the craters post analysis, we cannot rule out contamination in this case. On the other hand, EPMA data show that the alloy in this sample contains significantly lower N (3.54 wt%) than the glass. This implies that contamination by the alloy would lead to underestimation of N content in the glass (i.e., a lower $^{14}N^+/^{30}Si^+$ ratio), barring a matrix effect. Moreover, the high reproducibility (4.7%, 2*s*) of the three O^- beam SIMS analyses on this sample argues against non-systematic contamination.

Figure 7b show the most scatter of the three plots, which stands in contrast to the corresponding $^{12}C^{14}N^-/^{30}Si^-$ data for the Fe-free glasses (Fig. 5b). The York regression applied to the data has a poor mean square weighted deviation (MSWD = 43) and an OLS regression (not constrained to pass through the origin) has an r^2 value of 0.85 ($p < 0.001$). Comparison with the York regression applied to Fe-free glass data is difficult to see in Figure 7b, as that line is nearly coincident with one of the 95% confidence interval lines shown on the graph (i.e., the two regressions agree just barely within mutual uncertainties). The reasons for scatter in the Fe-bearing glass again are unclear. One concern is that the useful ion yield of $^{12}C^{14}N^-$ may depend on the

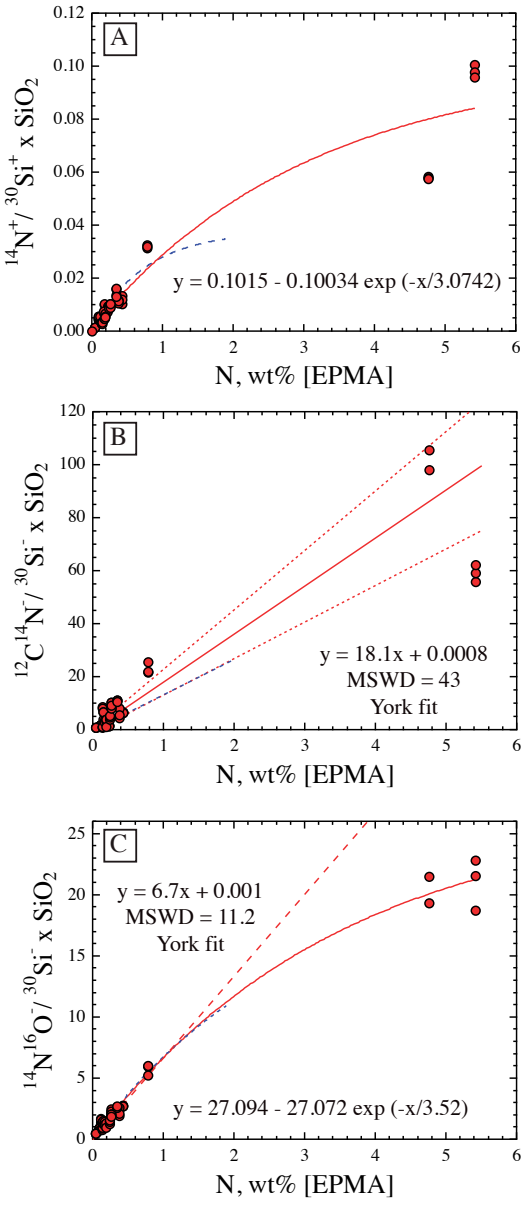

FIGURE 7. SIMS data for Fe-bearing glasses plotted against N contents determined by EPMA. Ratios are normalized for SiO_2 content determined by EPMA. In contrast to Figure 5, these plots show individual analyses. Consequently, the uncertainties for SIMS data ($2s_{\bar{X}}$ for each analysis) are within the symbol size. The point at the origin in each graph represents GRR1017 forsterite, used for blank correction. (**a**) $^{14}N^+/^{30}Si^+$ data. The solid curve is an exponential fit to the glass data with the equation shown; the dashed curve is fit to Fe-free glass data shown in Figure 5a. (**b**) $^{12}C^{14}N^-/^{30}Si^-$ data. The solid line is a York fit with the equation shown; dotted lines denote 95% confidence interval. The dashed line that is essentially coincident with the confidence interval on the right side of the graph is the fit to the Fe-free glass data shown in Figure 5b. (**c**) $^{14}N^{16}O^-/^{30}Si^-$ data. The solid curve is an exponential fit to the glass data with the equation shown. The dashed curve that is essentially coincident with that fit is the fit to Fe-free glass data shown in Figure 5c. The dashed line is a York fit to the Fe-bearing glass data with the equation shown; 95% confidence intervals are not shown, for the sake of clarity. (Color online.)

amount of C dissolved in the glass (Regier et al. 2016). However, we have found no systematic relationship between ^{12}C (used to calculate C concentrations) and $^{12}C^{14}N$ counts.

The $^{14}N^{16}O^-/^{30}Si^-$ data (Fig. 7c) are best fit with an exponential function, which is nearly coincident with the regression applied to the Fe-free data. We show a linear (York) regression for comparison, but this regression widely misses data for the two highest N concentration samples. An OLS regression (not shown) yields a reasonable fit ($r^2 = 0.98$, $p < 0.001$), but an unreasonable y-intercept (0.85).

Metal alloys

SIMS data for the Fe-N-C alloys (Table 4) are plotted in Figure 8. $^{14}N^+/^{54}Fe^+$ and N concentration are positively correlated. However, the York fit shown in Figure 8 has a poor MSWD (56); an OLS regression (not shown), unconstrained to pass through the origin, has an r^2 value of 0.87 ($p < 0.001$). The scatter in the data may in part reflect two problems. First, some of the alloys have complicated exsolution textures (Dalou et al. 2017a), which may have resulted in imprecise sampling of the bulk N content by our SIMS raster (with an analytical spot size larger than the exsolved features). Second, we were not able to obtain as many analyses of the alloys as for the glasses, owing to the variation in size and distribution of the alloy domains in different experiments. For instance, some experiments contained relatively abundant alloy spheres smaller than the spot size of the SIMS raster while others contained a much smaller amount of larger spheres, with space for only one raster area per sphere. Furthermore, three analyses were rejected because count rates ($^{54}Fe^+$ relative to $^{30}Si^+$) and post-SIMS SE imaging indicated contamination with silicate glass.

Whereas useful ion yields again cannot be calculated from our data, relative yields of $^{14}N^+$ between the Fe-free silicate glasses and alloys can be compared under the same beam conditions (O^- primary beam at MRP = 1250). Taking into account the scatter of the alloy data and the uncertainty involved in the non-linear

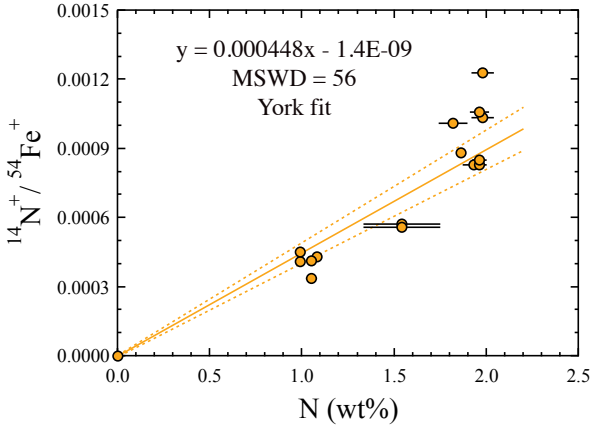

FIGURE 8. SIMS data for metals, showing $^{14}N^+/^{54}Fe^+$ as a function of N determined by EPMA. The point at the origin represents Fe metal, used for blank correction. Error bars for EPMA data (2*s*) not shown are within symbol size; error bars for SIMS data ($2s_{\bar{X}}$ for each individual analysis) are within the symbol size. The solid line is a York fit with the equation shown; dotted lines denote 95% confidence interval. (Color online.)

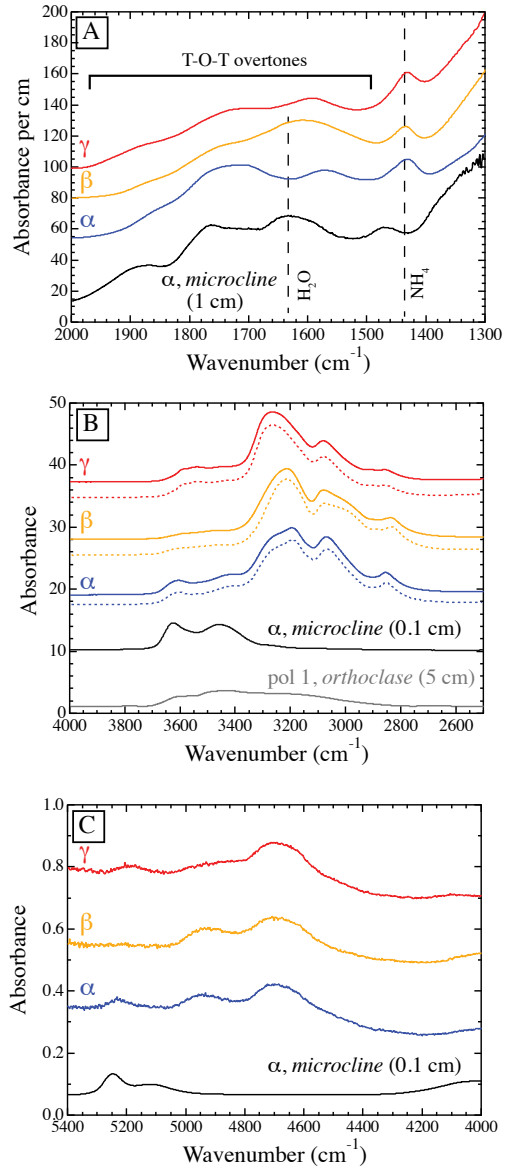

Figure 9. Polarized FTIR spectra of hyalophane compared to other feldspars. Spectra are offset for clarity. Corresponding polarization directions are labeled directly above each spectrum. All spectra of hyalophane are normalized to 1 cm path length, but spectra of other feldspars are normalized to other path lengths (as labeled) for the sake of comparison. (**a**) Mid-infrared spectra showing NH_4 bending mode (labeled with dashed line) and Si-O/Al-O (T-O-T) overtone bands in hyalophane. The bending mode for H_2O in microcline is also labeled. (**b**) Mid-infrared spectra showing fundamental N-H and O-H stretching vibrations in hyalophane. Solid lines are spectra taken on the crystal in this study. Dashed lines are spectra scanned from Beran et al. (1992), normalized to 1 cm thickness for comparison. Also shown are selected spectra of orthoclase (polarization 1 for GRR752 from Mosenfelder et al. 2015; normalized to 5 cm) and microcline (GRR1281 from Johnson and Rossman 2003; normalized to 0.1 cm). Spectra are shown without baseline correction except for GRR752, which was corrected. (**c**) Near-infrared spectra of hyalophane showing combination stretching + bending bands. Also shown for comparison is a polarized spectrum of microcline from Johnson and Rossman (2003), normalized to 0.1 cm. (Color online.)

relationship between $^{14}N^+/^{30}Si^+$ and N for the glasses, the yields are comparable: the $^{14}N^+$ yield for alloys ranges from 12 to 22 cps/(nA × wt% N), compared to 15 cps/(nA × wt% N) for B701.

Hyalophane

Our major element and nitrogen EPMA data (Table 1) agree within mutual uncertainties with the values presented by Beran et al. (1992) for another crystal from this locality. In particular, our average, blank-corrected N content for seven analyses of 0.113 ± 0.015 wt% (1*s*) compares well to Beran et al.'s value of 0.12 wt%. This amount of N corresponds to 0.15 wt% NH_4 (if all N is assumed to be incorporated in this form) or 0.29 wt% H_2O (if all H is assumed to be incorporated as NH_4).

FTIR spectra of hyalophane are shown in Figure 9. The band at ~1430 cm^{-1} (Fig. 9a) corresponds to the bending mode of NH_4^+, as seen in other N-bearing silicate minerals (e.g., Harlov et al. 2001; Watenphul et al. 2009, 2010). Other, broader bands in this region can be attributed to overtones of Si-O and Al-O stretching vibrations, as seen in the spectrum of microcline shown for comparison. A relatively broad band at ~1630 cm^{-1}, corresponding to the bending mode of H_2O, is present in microcline but not clearly seen in the hyalophane spectra.

Mid-IR spectra in Figure 9b for the crystal that we studied are identical within uncertainties to those published by Beran et al. (1992). The most prominent bands in all three polarizations, between ~3350 and 2800 cm^{-1}, represent NH_4^+ incorporated in the structure. Bands at higher wavenumbers (from ~3650 to 3400 cm^{-1}) resemble those found in orthoclase and microcline (Johnson and Rossman 2003), also shown in Figure 9b (with scale adjustments for the sake of comparison). In alkali feldspars, these bands are attributed to structurally incorporated H_2O (Johnson and Rossman 2003), but type IIa OH (as defined by Johnson and Rossman 2003) may also be present, contributing to the total absorption in the N-H stretching region.

The NIR spectra for hyalophane resemble those of NH_4^+-bearing microcline (Solomon and Rossman 1988), with three distinct bands. A band between ~5200 and 5250 cm^{-1} in all three spectra is attributed to the combination of bending and stretching vibrations for structurally bound H_2O, although evidence for the bending mode (Fig. 9a) is lacking as noted above. The other two bands (at ~4690 and 4940 cm^{-1}) presumably are combination bending and stretching bands for NH_4^+, although the middle band is at a higher frequency than expected for this combination.

SIMS analyses obtained at ASU for hyalophane are shown in Figure 5. Two analyses with the O^- beam yielded a value of $^{14}N^+/^{30}Si^+ = 0.000056 \pm 0.000008$ (2*s*), which falls significantly to the right of the curve for the Fe-free glasses in Figure 5a (after normalizing for SiO_2 content). $^{12}C^{14}N^-/^{30}Si^-$ from three analyses was below the detection limit, but the value for $^{14}N^{16}O^-/^{30}Si^-$ (0.0026 ± 0.0002, 2*s*) was highly reproducible and about seven times the blank. This ratio also falls significantly to the right of the curve for the Fe-free glasses (Fig. 5c). The offsets for hyalophane in Figure 5a and 5c suggest a significant matrix effect for N, perhaps owing to the high atomic mass of Ba (the matrix contains ~20 wt% BaO; Table 1); the effect is greater for the Cs^+ beam analyses.

Three additional SIMS analyses were obtained on the same hyalophane crystal at Caltech during a session in which we cali-

brated for H and F in plagioclase, using the same feldspar and F-bearing glass standards used in Mosenfelder et al. (2015); the primary data are provided in the supplementary material. Total contents of H_2O (620 ± 31 μg/g, 2*s*) and F (109 ± 35 μg/g, 2*s*) were calculated from $^{16}O^1H^-/^{18}O^-$ and $^{19}F^-/^{18}O^-$, respectively. The F concentration represents the highest amount we have measured to date in a feldspar (cf. Mosenfelder et al. 2015). The value for H_2O is substantially lower than the equivalent amount of H_2O (0.29 wt%) calculated above from the N concentration measured by EPMA. That calculation assumes NH_4^+ as the only H-bearing species, which underestimates the contribution to the $^{16}O^1H^-$ yield from O-H species. As with N, we attribute this discrepancy to a significant matrix effect.

Discussion

Incorporation mechanisms for C-O-H-N in glasses

Previous studies suggest a plethora of solubility mechanisms for C-O-H-N species in silicate melts under reduced conditions (e.g., Chi et al. 2014; Armstrong et al. 2015; Li et al. 2016a). The following discussion focuses primarily on N incorporation and hinges on a comparison of our combined spectroscopic and chemical data for the Fe-free glasses to results from other studies. Possible species responsible for accommodating N dissolution include molecular N_2 or NH_3, NH_4^+, NH_2^-, NH_2^+, NH^{2-}, CN^-, nitrosyl complexes (e.g., X-N-O or X-N=O, where X represents a metal cation), and $X\text{-}N^{3-}$ (i.e., nitride complexes). Assignments of these species (Mulfinger 1966; Schwerdtfeger et al. 1978; Ito and Fruehan 1988; Libourel et al. 2003; Roskosz et al. 2006; Mysen et al. 2008; Mysen and Fogel 2010; Kadik et al. 2011, 2013, 2015, 2016) have been based on spectroscopy and/or thermodynamic considerations; in our case, we use FTIR and simple mass balance constraints to infer incorporation mechanisms. Supplemental[1] Table S1 contains a summary of our interpretations.

C speciation. Definitive constraints on C speciation in reduced glasses cannot be derived from our new data. Overall, the C contents of the Fe-free glasses are very low. In contrast to some previous studies from our lab on basaltic glasses under reduced conditions (Stanley et al. 2014; Armstrong et al. 2015), we see no spectroscopic evidence for C-O complexes of any type. Furthermore, we see no hints of C-N bonding. C≡N bonds would give rise to strong stretching vibrations in the vicinity of 2250 cm^{-1} (Smith 1999). C-N stretching vibrations are characterized by weaker bands between 1400 and 1000 cm^{-1} (Smith 1999), which are also not observed in our spectra, although the samples are too thick to see absorptions below ~1250 cm^{-1}. Given these negative results, we suggest that the C in our glasses is dissolved as CH_4 or CH_3^-, which are more easily detected by Raman spectroscopy than FTIR at these low concentration levels (Ardia et al. 2013). This inference is consistent with the work of Ardia et al. (2013) on a nominally Fe-free basaltic composition and with the volatile speciation map derived by Armstrong et al. (2015), given the high H/C ratios of the glasses compared to most of those synthesized by Stanley et al. (2014) and Armstrong et al. (2015). The discrepancy between the positive and negative correlations between C and N (Fig. 4a) in the Fe-free and Fe-bearing glasses, respectively, could result from more complicated C speciation (e.g., C≡O species in addition to CH_4/CH_3^-) in the latter samples, but this explanation is speculative in light of difficulties in absolute quantification of the various species by Raman spectroscopy.

We note that attributions of bands at ~3200 cm^{-1} and ~2350 cm^{-1} by Kadik et al. (2016) to C-N and CO_2, respectively, are not supported by other literature data. The band at ~3200 cm^{-1} forms an indistinct shoulder on the main O-H band in their samples, and is at too high a frequency for C-N or C≡N. In the case of the 2350 cm^{-1} band, the observed doublet is clearly a signature of gas-phase CO_2 in the beam path (characterized by peak splitting resulting from the combination of rotational modes with the asymmetric stretching vibration), rather than CO_2 dissolved in a glass (characterized by a single peak; e.g., Fine and Stolper 1985).

N-H speciation. To identify possible N-H species in the glasses, we use information from both the MIR (Figs. 3b–d) and NIR (Fig. 3a). With increasing N content, the intensity of the O-H band at ~3550 cm^{-1} decreases while N-H bands with similar shapes increase in intensity (Figs. 3b and 3d). Four peaks can be discerned in the glasses with 0.22 to 1.84 wt% N, at ~3370, 3285, 3225, and 3187 cm^{-1} (Fig. 3d). The most intense of these absorptions shows a slight, continuous shift in peak location with increasing N content (from 3370 cm^{-1} down to 3353 cm^{-1}). This shift could represent modulation of N-H stretching by hydrogen bonding (i.e., N-H…N, which would increase with increasing N content), or a subtle difference in populations of different N-H species. Otherwise, the similarity in peak locations in all of the spectra suggests that all the glasses contain the same N-H species. However, differences in the region between 1400 and 1700 cm^{-1} (Fig. 3c) as well as in the NIR (Fig. 3a) lead us to a more nuanced interpretation.

A very weak band at 1440 cm^{-1} is present at lower N concentrations (in B703 and B704; Fig. 3c) that could correspond to the bending motion of NH_4^+. However, distinct bands in the region normally associated with NH_4^+ stretching (between ~2800 and 3200 cm^{-1}; Fig. 9) are not present. This contrasts with glasses made in the system $FeO\text{-}Na_2O\text{-}Al_2O_3\text{-}H_2O$ ± C under reducing conditions by Kadik et al. (2013, 2015, 2016) that clearly contain NH_4^+, with peak heights decreasing monotonically with decreasing f_{O_2} but evident even at ΔIW as low as –3.3. The prevalence of NH_4^+ in those glasses, as opposed to this study, is perhaps best ascribed to differences in bulk composition; f_{O_2} is unconstrained in our experiments but is likely in a similar range, with similar amounts of Si_3N_4 having been added to capsules.

A more intense band in this region is present at 1615 cm^{-1}. At higher N contents, it replaces a band at 1635 cm^{-1} (in B703 and B704) that is attributed to the H_2O bending mode (e.g., Stolper 1982). A band at similar frequency (1612–1619 cm^{-1}) was previously assigned by Kadik et al. (2013, 2015, 2016) to the bending mode for H_2O, but this interpretation is inconsistent with any other study on H_2O-containing glasses as well as with the fact that the band is present even when there are few or no O-H stretching vibrations (Fig. 3b; see also Fig. 5d in Kadik et al. 2013). Stanley et al. (2014) speculated that the 1615 cm^{-1} band was caused by C = O stretching in a complex such as an amide, while noting a correlation between peak heights at 1615 and 3370 cm^{-1}. A simpler explanation is that the band at 1615 cm^{-1} represents N-H bending, with or (more likely) without C present. In particular, the NH_2^- functional group gives

rise to a strong in-plane H-N-H bending ("scissors") motion at 1650–1620 or 1650–1580 cm^{-1} for primary amides and amines, respectively (Smith 1999). Attribution of the band at 1615 cm^{-1} to NH_2^- bending is consistent with the assignment by Mysen et al. (2008) of vibrations at 3400 and 3280 cm^{-1} in Raman spectra to NH_2^- stretching modes; we interpret IR-active bands at similar frequencies (3370 and 3225 cm^{-1}) to represent NH_2^- asymmetric and symmetric stretching vibrations, respectively. Furthermore, the band at 4965 cm^{-1}, present in all of our spectra (Fig. 3a), can then be assigned to a combination of NH_2^- bending and stretching vibrations. This band is in between the well-known (e.g., Stolper 1982) combination bands observed in hydrous glasses at ~5200 cm^{-1} (combination of stretching and bending for H_2O) and ~4500 cm^{-1} (combination of stretching motions for O-H and X-OH), and thus cannot be attributed to either of those species. Other bands in the NIR are discussed below.

At higher N contents, a new band arises with a peak at 1530 cm^{-1} (in detail the band structure in this frequency region is complex, with at least two bands needed to explain the asymmetry of the absorption). As with the 1615 cm^{-1} band, this band is also correlated with the appearance of a new peak in the NIR (at 4840 cm^{-1}). We speculate that the 4840 cm^{-1} band is a combination of N-H stretching at 3285 cm^{-1} with bending at 1530 cm^{-1}, and specifically that the species is NH^{2-}, attached to the silicate network of the glass. Using a similar analogy as for NH_2^-, we note that the in-plane bending motion of NH^{2-} in secondary amides occurs between 1570 and 1515 cm^{-1} (Smith 1999). A band at 1530 cm^{-1} could also be an overtone of Si-N stretching at ~800 cm^{-1} (Soignard and McMillan 2004), but this would not explain the combination band at 4840 cm^{-1}. The highly reduced species NH^{2-} was presumed by Mulfinger (1966) to be present in glasses synthesized at low f_{O_2} in the system SiO_2-CaO-Na_2O-B_2O_3-H_2, but to our knowledge has not been considered in the Earth science literature.

Our assignment of the NH^{2-} species runs counter to the idea promoted by Mysen et al. (2008) and Mysen and Fogel (2010) that a Raman band in reduced glasses at 3310–3320 cm^{-1} corresponds to isolated NH_3 molecules. This assignment was based on the relatively narrow width of the peak and similar frequency to the strongest vibration in gaseous NH_3 (at ~3335 cm^{-1}; Nakamoto 2009a). Kadik et al. (2013, 2015, 2016) applied this interpretation in their assignment of the 3285 cm^{-1} IR band to NH_3. Our explanation is consistent with N-H stretching at a single frequency (for the single N-H bond in NH^{2-}) as well as with the presence of an apparent bending motion and combination band. Isolated NH_3 molecules should exhibit a degenerate deformational mode at 1627 cm^{-1} (e.g., Nakamoto 2009a, p. 175), which is not observed in our spectra (Fig. 3c; the band at 1635 cm^{-1} in B703 and B704 is clearly the bending mode of H_2O). On the other hand, NH_3 could be incorporated structurally within the silicate network in the form of a metal-ammine complex. The NH_3 ligand in metal-ammine complexes gives rise to two stretching vibrations, two deformational modes, and one rocking vibration (Nakamoto 2009b). The band at 1615 cm^{-1} could be assigned to the degenerate deformational mode. However, the band at 1530 cm^{-1} is not easily assigned to either deformational mode, based on comparison to frequencies of known metal-ammine complexes (Nakamoto 2009b). Nevertheless, this is a possible incorporation mechanism in glasses that should be amenable to further study using a combination of IR and Raman spectroscopy.

In addition to the band at 4107 cm^{-1}, attributed to dissolved H_2 (Hirschmann et al. 2012), three other bands are present in NIR spectra of our glasses with higher N contents. Whereas one band at 4600 cm^{-1} rises at the expense of the X-O-H combination band at 4500 cm^{-1} and is correlated in intensity with the band at 4965 cm^{-1}, two weaker bands at ~4300 and 4200 cm^{-1} are present only at the highest N contents and appear in association with the band at 4840 cm^{-1}. The origin of these bands is harder to fingerprint but we speculate that they correspond to combinations of N-H stretching and X-NH stretching, by analogy with the X-O-H combination band (the frequencies of X-NH stretching cannot be determined from our data). In this scenario, the band at 4600 cm^{-1} would represent NH_2^- groups while the other two bands are associated with NH^{2-}. Combinations of N-H stretching with out-of-plane (wagging) H-N-H or N-H bending motions are also possible but seem unlikely as those vibrations are typically weak and occur at frequencies too low to explain this combination (600 to 750 cm^{-1}; Smith 1999).

The above explanation of the N-H vibrations does not account for the weak band seen at 3187 cm^{-1} (Fig. 3d). One possibility is that this vibration is an overtone of the bending motion at 1615 cm^{-1}. Harlov et al. (2001) made an analogous assignment for the bending motion of NH_4^+ in buddingtonite. Bands at this frequency (between 3180 and 3185 cm^{-1}; Kadik et al. 2016) as well as a Raman band at ~2915 cm^{-1} (Mysen et al. 2008; Kadik et al. 2011) have also been assigned to the relatively oxidized species NH_2^+. The assignment of the Raman band is based on speculation by Mysen et al. (2008), but we note that Raman bands at this frequency could equally well result from C-H stretching (particularly in the experiments performed by Kadik et al. in the presence of graphite and H_2). Furthermore, the assignment of the band at ~3185 cm^{-1} to NH_2^+ is not well justified by comparison to known compounds containing this functional group (such as hydroxylamine; Kowal 2002).

Other mechanisms for N incorporation. We infer that substantial amounts of one or more N-bearing species unattached to hydrogen are present in some samples. B710 and B711 have similar peak heights corresponding to N-H vibrations in the MIR (Figs. 3b and 3d) and NIR (Fig. 3a) despite a factor of more than two difference in their total N contents. Moreover, the decline in H contents in both the Fe-free and Fe-bearing glasses with increasing N content (Figs. 4b and 6) requires the presence of N-bearing species unattached to hydrogen, to satisfy mass balance. For example, B711 contains 0.67 wt% H_2O and 1.89 wt% N, corresponding to an H/N ratio of 0.55 (Table 3). Even neglecting the fact that H_2 is present in this glass (as evident from the peak at 4107 cm^{-1}), there is thus not enough H to account for all the nitrogen by the mechanisms discussed above. This imbalance is also evident for several Fe-bearing samples with high N contents (and low H/N), as listed in Table 3 (e.g., B712b, B712d, B714c, and B714e).

Having already dismissed C-N or C≡N as being significant species in our glasses, we next consider molecular N_2 (trapped in the silicate network), N-O, and N^{3-} attached directly to the silicate network. N_2, which is not infrared-active, is likely to be present in some of the Fe-free glasses. Attempts to obtain Raman

spectra on these glasses were foiled by fluorescence, but the Fe-bearing glasses do show a characteristic peak for dissolved N_2 that is distinct from atmospheric N_2 (Dalou et al. 2017b). The presence of N_2 even at extremely reduced conditions is somewhat surprising, but consistent with other studies (Mysen et al. 2008; Mysen and Fogel 2010; Kadik et al. 2011, 2013, 2015).

Nitrogen can also be bound in other complexes unassociated with hydrogen. Roskosz et al. (2006) presented evidence from Raman and NMR spectroscopy of high-pressure silicate melts for nitrosyl complexes (e.g., Si-N-O), in addition to N_2. However, their experiments were performed under conditions likely more oxidizing than other studies, owing to the different nitrogen source used (AgN_3) and lack of an O_2 or H_2 buffer. Although it is unclear whether the Raman bands (at ~2100 and 2200 cm^{-1}) attributed by Roskosz et al. (2006) to nitrosyl are IR-active, we do not observe them in our samples. We also see no evidence for NO_2 groups, which are characterized in organic compounds by strong asymmetric and symmetric stretching vibrations at ~1500 and 1350 cm^{-1}, respectively (Smith 1999).

The formation of nitride complexes ($X\text{-}N^{3-}$) in silicate glasses has been studied extensively under reducing conditions at 1 atm (Mulfinger 1966; Schwerdtfeger et al. 1978; Ito and Fruehan 1988; Libourel et al. 2003). These studies infer either from direct measurements or thermodynamic calculations that the solubility of nitrides dwarfs that of cyanide complexes. The presence of certain cations may also promote the formation of nitride complexes; in particular, Ti^{4+}—reduced to Ti^{3+} at very low f_{O_2}—may have a strong affinity for N (Libourel et al. 2003). All of our glasses contain sufficient amounts of TiO_2 (up to 1 wt%) for this mechanism to be relevant. Mysen et al. (2008) and Mysen and Fogel (2010) dismissed nitrides (and azides) as an incorporation mechanism in their high-pressure glasses, based on the lack of detectable stretching vibrations at the appropriate frequencies in Raman spectra. However, their experiments were conducted at oxygen fugacities ($\Delta IW \geq 0$) substantially higher than our most reduced experiments. This mechanism in fact could be the primary mode of incorporation for N under truly anhydrous and reduced conditions, which are difficult to achieve in high-pressure experiments owing to infiltration of H into samples from assembly parts.

Processes in SIMS

The processes that lead to "matrix effects" in SIMS are still poorly understood for complex silicate materials, compared to simpler systems such as metals (e.g., Williams 1979). Regier et al. (2016) have provided the most comprehensive study of this topic to date for nitrogen in silicates, but our results suggest additional complexities that have implications for other studies that assume linear calibrations and a lack of matrix effects.

Regier et al. (2016) documented contrasting effects of total H_2O ($OH + H_2O$) content on useful ion yields of $^{14}N^+$ and $^{14}N^{16}O^-$ in rhyolitic vs. basaltic glasses. In the case of N^+ analysis, useful ion yields went up for rhyolites and down for basalts with increasing H_2O content. However, the RSF measured by Regier et al. (2016) was unchanged from 0 to 2 wt% H_2O, which spans the range of total H_2O contents covered by our samples. For our very N-rich samples (compared to Regier et al. 2016), a non-linear fit is demanded when N is greater than ~1000 μg/g. This result contrasts with the linear calibration for N in clays established by Williams et al. (2012), although Williams et al. (2013) observed curvature at higher N concentrations. Furthermore, Hervig et al. (2014) observed a strong non-linearity between 2 and 5 wt% N in the N^+ signal in a suite of oxynitride glasses.

The cause of non-linearity in these working curves is unknown, but one possibility is that secondary ion yields are affected by differences in N speciation. The formation of N^+, NO^-, or CN^- secondary ions requires both sputtering and ionization, and sputtering is fundamentally influenced by primary ion impact energy, the masses of the atoms that participate in the cascade of collisions that occur following impact, and surface binding energies (e.g., Van der Heide 2014). Regarding the latter effect, we might expect that higher bond energies of nitride ($X\text{-}N^{3-}$) complexes (which we have proposed become increasingly important in our glasses at high N contents) compared to N-H species would lead to a decrease in sputter yield. On the other hand, our intuition is that this influence of surface binding energies is subsidiary to the first two factors because the energy of the impacting primary ions is orders of magnitude higher than local bond energies. Models of the SIMS process predict whole scale rearrangement of the surface prior to ejection of ions, so the local environment of N atoms can change drastically; this surface rearrangement logically facilitates the recombination process producing molecular ions such as CN^- that were not present in the substrate prior to bombardment. Furthermore, such an explanation for the changes in RSF would not easily explain similar non-linear working curves documented for H_2O in glasses measured using H^- (Hauri et al. 2002; Hervig et al. 2003; Aubaud et al. 2007), H^+ (Singer et al. 2014), and OH^- (Tenner et al. 2009; Mosenfelder et al., unpublished data) secondary ions. Non-linear effects have also been seen for major elements in olivine and pyroxene (Steele et al. 1981). The concentration-dependent curvature in our SIMS data may, therefore, be unrelated to speciation in the undisturbed glasses, and/or may represent an effect of the ionization process along with rearrangement of target atoms following primary ion bombardment. Distinguishing these effects in future studies will be a major challenge.

Our linear and precise working curve for $^{12}C^{14}N^-$ in the C-poor, Fe-free glasses (Fig. 5b) seemingly contradicts the conclusion of Regier et al. (2016) that high and relatively constant C contents are necessary to use this method. However, the critical difference between the two studies is that our glasses contain much more N than the natural melt inclusions studied by Regier et al. (2016), so the availability of C may be of secondary importance.

An ambiguity left by our study concerns the matrix effect of heavy elements on light element analysis. Significant matrix effects of this type have been documented for oxygen and hydrogen isotope analysis (Eiler et al. 1997; Hauri et al. 2006), but have yet to be conclusively demonstrated for hydrogen concentration measurements (Aubaud et al. 2007; Mosenfelder and Rossman 2013). We emphasize that a better understanding of the process requires measuring sputter yields (which can provide estimations of primary ion concentration in the crater floor) to separate the effects of matrix ions from primary ion implantation on the secondary collisions that lead to sputtering and ionization (Eiler et al. 1997). Nevertheless, the large range in Fe contents for the

Fe-bearing glasses (owing to variable amounts of added Fe_4N or Fe and precipitation of metal alloys) suggests an ideal test case for measuring such an effect, with Mg numbers ranging from 47 to 97 (where Mg no. = 100 × molar Mg/[Mg+Fe]). However, there is a weak anti-correlation ($r^2 = 0.38$, $p < 0.01$) between Mg no. and the slope of each individual point on our SIMS working curve for $^{14}N^{16}O^-/^{30}Si^-$ (Fig. 10). Correlations for the other curves are considerably worse. Furthermore, although we cannot directly compare the data sets, the relative yields of $^{14}N^+$ between the silicate glasses and alloys (with obviously high average molar mass) analyzed with an O^- primary beam are similar. Finally, our data on the Fe-free glasses in Figure 5a agree well with data for low-mass clays from Williams et al. (2012), up to 0.2 wt% N.

Taken together, these results suggest that the average molar mass of the matrix has little discernible effect on the ionization process. On the other hand, results on the single hyalophane sample (using both Cs^+ and O^- primary beams) suggest a significant effect for Ba, which is 2.5 times the mass of Fe. We have presented evidence for such a matrix effect not only for N but also for H; any effect on F is impossible to constrain from our data. The sense of the effect (a reduction in yield of the light element relative to the heavier reference mass with an increase in molar mass of the matrix) is consistent with results on H analysis of zircon via SIMS (Mosenfelder and Rossman 2014 and unpublished data) and with instrumental mass fractionation of light and heavy isotopes of O (Eiler et al. 1997) and H (Hauri et al. 2006). Further work including measurement of sputter yields is needed to assess the relative importance of heavy matrix ions as opposed to implanted primary ions in ionization processes relevant to volatile element analysis.

Implications

Our conclusion on N incorporation mechanisms in basaltic glasses is that the main N-H species present under reduced conditions ($f_{O_2} < \Delta IW$) are NH_{2-} and NH^{2-}. However, at higher N concentrations, N_2 and nitride complexes may also be important. This complicates the conventional interpretation that N solubility increases with OH content dissolved in the melt (Kadik et al. 2016; Dalou et al. 2017a). Consequently, partitioning experiments at extremely reduced conditions may need to be revisited, because N may exhibit non-Henrian behavior owing to changes in incorporation mechanisms at lower N concentrations.

The occurrence of N_2 and nitride species in reduced glasses is applicable to many experiments conducted to explore N incorporation in silicate melts, which tend to have high N/H ratios (Kadik et al. 2013, 2015, 2016; Roskosz et al. 2013; Dalou et al. 2017a; this study). On the other hand, it may not be generally applicable to the speciation of magmatic N during terrestrial planetary accretion and differentiation, as molar N/H ratios in volatile-rich chondritic bodies and terrestrial planets are thought to be <<1 (Marty 2012; Halliday 2013; Hirschmann 2016). However, judging from enstatite chondrites, which have appreciable N and no detectable H (e.g., Grady et al. 1986; Halliday 2013), N_2 and nitride species could have had an important influence on nitrogen solubility and partitioning during melting of highly reduced inner planetary objects, including the aubrite parent body (Grady et al. 1986) and Mercury (Zolotov 2010).

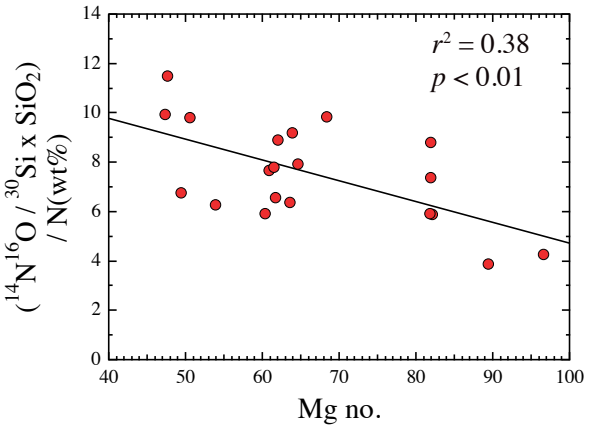

Figure 10. Evaluation of matrix effect for Fe-bearing glasses. Each point shown represents the slope of the corresponding data point in Figure 7c as a function of Mg no. (100 × molar Mg/[Mg+Fe]) of the glass. Only a weak correlation ($r^2 = 0.38$, $p < 0.01$) is evident. (Color online.)

This may also apply to delivery of volatiles to Earth in similarly reduced objects (Wohlers and Wood 2015).

The curvature demonstrated in our N^+ and NO^- SIMS data has implications for studies that estimate N concentrations by assuming linear calibrations. Mallik et al. (2018) pinned their linear calibration for N in rhyolites on their highest N concentration glass, despite large uncertainties associated with its measured N content and $(^{14}N^+ + {}^{15}N^+)/{}^{30}Si^+$ ratio, because of concerns about possible bias introduced by correction of the Bremsstrahlung background in their EPMA data at lower N contents. However, the data could also be reasonably fit to an exponential function similar to those we have demonstrated. The calibration curve shown by Li et al. (2015) also could be treated with a non-linear fit, rather than forcing a linear fit through the origin, but data scatter prevents an unambiguous interpretation in this case. Therefore, future studies should take into account the possibility of changes in RSF akin to those demonstrated in this study, particularly for ranges in N concentration and analytical conditions similar to ours.

On the one hand, our results suggest that ignoring matrix effects for N analysis associated with low-H_2O bulk compositions (cf. Regier et al. 2016) is a reasonable approximation, to first order. On the other hand, the results on hyalophane emphasize the need to use matrix-matched standards whenever possible when analyzing volatile contents in particularly heavy matrices. Thus, for example, the SIMS measurements of H in Ba-containing alkali feldspars from a lunar sample by Mills et al. (2017) might be affected by the matrix when using low-Ba reference materials. Our limited results suggest that, for nitrogen, the matrix effect is more severe when a Cs^+ primary beam is used and negative ions (e.g., NO^-) are collected. However, we concur with Regier et al. (2016) that this methodology may be preferable when an instrument with sufficient transmission is available; despite the lower useful ion yield for NO^- compared to N^+ (Regier et al. 2016), our results support the conclusion that higher overall count rates can be achieved as a result of the higher sputter yield of a high-current Cs^+ primary beam compared to O^-.

ACKNOWLEDGMENTS

This work was supported by NSF grants EAR-1426772, AST-1344133, and EAR-1322082. The National ASU SIMS facility is supported by NSF EAR-1352996. We gratefully acknowledge Lynda Williams and Margo Regier for assistance with SIMS at ASU and Yunbin Guan for assistance with SIMS at Caltech. The manuscript was improved by reviews from Michael Wiedenbeck, associate editor Adam Kent, and an anonymous referee. We also thank Andrew Locock for providing the hyalophane sample. This paper is dedicated to Erik Hauri, who was an inspirational geochemist and a pioneer in the use of SIMS for measuring volatile elements in geological materials.

REFERENCES CITED

Ardia, P., Hirschmann, M.M., Withers, A.C., and Stanley, B.D. (2013) Solubility of CH_4 in a synthetic basaltic melt, with applications to atmosphere–magma ocean–core partitioning of volatiles and to the evolution of the Martian atmosphere. Geochimica et Cosmochimica Acta, 114, 52–71.

Armstrong, L.S., Hirschmann, M.M., Stanley, B.D., Falksen, E.G., and Jacobsen, S.D. (2015) Speciation and solubility of reduced C-O-H-N volatiles in mafic melt: Implications for volcanism, atmospheric evolution, and deep volatile cycles in the terrestrial planets. Geochimica et Cosmochimica Acta, 171, 283–302.

Aubaud, C., Withers, A.C., Hirschmann, M., Guan, Y., Leshin, L.A., Mackwell, S., and Bell, D.R. (2007) Intercalibration of FTIR and SIMS for hydrogen measurements in glasses and nominally anhydrous minerals. American Mineralogist, 92, 811–828.

Bastin, G.F., and Heijligers, H.J.M. (1991) Quantitative electron probe microanalysis of nitrogen. Scanning, 13, 325–342.

Bastin, G.F., Dijkstra, J.M., and Heijligers, H.J.M. (1998) PROZA96: an improved matrix correction program for electron probe microanalysis, based on a double Gaussian $\Phi(\rho z)$ approach. X-Ray Spectrometry, 27 (1):3–10.

Beran, A., Armstrong, J., and Rossman, G.R. (1992) Infrared and electron microprobe analysis of ammonium ions in hyalophane feldspar. European Journal of Mineralogy, 4, 847–850.

Burdo, R.A., and Morrison, G.H. (1971) Table of atomic and molecular lines for spark source mass spectrometry of complex sample-graphite mixes. Report no. 1670. Materials Science Center, Cornell University, Ithaca, New York.

Carnera, A., Mazzoldi, P., Boscolo-Boscoletto, A., Caccavale, F., Bertoncello, R., Granozzi, G., Spagnol, I., and Battaglin, G. (1990) On the formation of silicon oxynitride by ion implantation in fused silica. Journal of Non-crystalline Solids, 125, 293–301.

Chantler, C.T., Olsen, K., Dragoset, R.A., Kishore, A.R., Kotochigova, S.A., and Zucker, D.S. (2005) X-ray Form Factor, Attenuation, and Scattering Tables (ver. 2.1). National Institute of Standards and Technology, Gaithersburg, Maryland.

Chen, J., Schauer, S., and Hervig, R. (2013) Normal-incidence electron gun alignment method for negative ion analysis on insulators by magnetic sector SIMS. Nuclear Instruments and Methods in Physics Research B, 295, 50–54.

Chi, H., Dasgupta, R., Duncan, M.S., and Shimizu, N. (2014) Partitioning of carbon between Fe-rich alloy melt and silicate melt in a magma ocean—implications for the abundance and origin of volatiles in Earth, Mars, and the Moon. Geochimica et Cosmochimica Acta, 139, 447–471.

Dalou, C., Hirschmann, M.M., von der Handt, A., Mosenfelder, J., and Armstrong, L.S. (2017a) Nitrogen and carbon fractionation during core-mantle differentiation at shallow depth. Earth and Planetary Science Letters, 458, 141–151.

Dalou, C., Le Losq, C., Hirschmann, M.N., Jacobsen, S.D., and Füri, E. (2017b) Evolution of C-O-H-N volatile species in the magma ocean during core formation. American Geophysical Union, Fall Meeting 2017, abstract V31E-01.

De Gregorio, B.T., Stroud, R.M., Cody, G.D., Nittler, L.R., David Kilcoyne, A.L., and Wirick, S. (2011) Correlated microanalysis of cometary organic grains returned by Star- dust. Meteoritics and Planetary Science, 46, 1376–1396.

Dekas, A.E., Poretzky, R., and Orphan, V. (2009) Deep-sea Archaea fix and share nitrogen in methane consuming microbial consortia. Science, 326, 422–426.

Divljan, S.B. (1954) The finding of hyalophane near Busovaca in central Bosnia. Recueil des Travaux de L'institut de Geologie "JovanZujovic", 7, 269–275.

Donovan, J.J., Lowers, H.A., and Rusk, B.G. (2011) Improved electron probe microanalysis of trace elements in quartz. American Mineralogist, 96, 274–282.

Eiler, J.M., Graham, C., and Valley, J.W. (1997) SIMS analysis of oxygen isotopes: matrix effects in complex minerals and glasses. Chemical Geology, 138, 221–244.

Fine, G., and Stolper, E. (1985) Dissolved carbon dioxide in basaltic glasses: concentrations and speciation. Earth and Planetary Science Letters, 76, 263–278.

Fitzsimons, I.C.W., Harte, B., Chinne, I.L., Gurney, J.J., and Taylor, W.R. (1999) Extreme chemical variation in complex diamonds from George Creek, Colorado: a SIMS study of carbon isotope composition and nitrogen abundance. Mineralogical Magazine, 63, 857–878.

Grady, M.M., Wright, I.P., Carr, L.P., and Pillinger, C.T. (1986) Compositional differences in enstatite chondrites based on carbon and nitrogen stable isotope measurements. Geochimica et Cosmochimica Acta, 50, 2799–2813.

Halliday, A.N. (2013) The origins of volatiles in the terrestrial planets. Geochimica et Cosmochimica Acta, 105, 146–171.

Harlov, D.E., Andrut, M., and Pöter, B. (2001) Characterisation of buddingtonite $(NH_4)[AlSi_3O_8]$ and ND_4-buddingtonite $(ND_4)[AlSi_3O_8]$ using IR spectroscopy and Rietveld refinement of XRD spectra. Physics and Chemistry of Mineral 2, 28, 188–198.

Hashizume, K. and Marty, B. (2004) Nitrogen isotopic analyses at the sub-picomole level using an ultra-low blank laser extraction technique. In P.A. Groot, Ed., Handbook of Stable Isotope Analytical Techniques, vol. 1, p. 361–375. Elsevier.

Hauri, E.H., Wang, J., Dixon, J.E., King, P.L., Mandeville, C., and Newman, S. (2002) SIMS analysis of volatiles in silicate glasses 1. Calibration, matrix effects and comparisons with FTIR. Chemical Geology, 183, 99–114.

Hauri, E.H., Shaw, A.M., Wang, J., Dixon, J.E., King, P.L., and Mandeville, C. (2006) Matrix effects in hydrogen isotope analysis of silicate glasses by SIMS. Chemical Geology, 235, 352–365.

Hervig, R.L., Mazdab, F.K., Moore, G., and McMillan, P.F. (2003) Analyzing hydrogen (H_2O) in silicate glass by secondary ion mass spectrometry and reflectance Fourier transform infrared spectroscopy. In: Devivo, B., Bodnar, R. (Eds.), Melt inclusions in volcanic systems: methods, applications, and problems. Developments in Volcanology. Elsevier, Amsterdam, pp. 83–103.

Hervig, R.L., Mazdab, F.K., Williams, P., Guan, Y., Huss, G.R., and Leshin, L.A. (2006) Useful ion yields for Cameca IMS 3f and 6f SIMS: limits on quantitative analysis. Chemical Geology, 227, 83–99.

Hervig, R.L., Fudge, C., and Navrotsky, A. (2014) Analyzing nitrogen in cordierites and other phases by SIMS. Goldschmidt Abstracts, 982.

Hirschmann, M.M. (2016) Constraints on the early delivery and fractionation of Earth's major volatiles from C/H, C/N, and C/S ratios. American Mineralogist, 101, 540–553.

Hirschmann, M.M., Withers, A.C., Ardia, P., and Foley, N.T. (2012) Solubility of molecular hydrogen in silicate melts and consequences for volatile evolution of terrestrial planets. Earth and Planetary Science Letters, 345, 38–48.

Humbert, F., Libourel, G., France-Lanord, C., Zimmermann, L., and Marty, B. (2000) CO_2-laser extraction-static mass spectrometry analysis of ultra-low concentrations of nitrogen in silicates. Geostandards Newsletter, 24, 255–260.

Ito, K., and Fruehan, R.J. (1988) Thermodynamics of nitrogen in CaO-SiO_2-$Al2O_3$ slags and its reaction with Fe-C_{sat} melts. Metallurgical Transactions B, 19B, 419–425.

Johnson, B., and Goldblatt, C. (2015) The Nitrogen Budget of Earth. Earth Science Reviews, 148, 150–173.

Johnson, E.A., and Rossman, G.R. (2003) The concentration and speciation of hydrogen in feldspars using FTIR and ^{1}H MAS NMR spectroscopy. American Mineralogist, 88, 901–911.

Kadik, A.A., Kurovskaya, N.A., Ignat'ev, Y.A., Kononkova, N.N., Koltashev, V.V., and Plotnichenko, V.G. (2011) Influence of oxygen fugacity on the solubility of nitrogen, carbon, and hydrogen in FeO-Na_2O-SiO_2-Al_2O_3 melts in equilibrium with metallic iron at 1.5 GPa and 1400°C. Geochemistry International, 49, 429–438.

Kadik, A.A., Litvin, Y.A., Koltashev, V.V., Kryukova, E.B., Plotnichenko, V.G., Tsekhonya, T.I., and Kononkova, N.N. (2013) Solution behavior of reduced N-H-O volatiles in FeO-Na_2O-SiO_2-Al_2O_3 melt equilibrated with molten Fe alloy at high pressure and temperature. Physics of the Earth and Planetary Interiors, 214, 14–24.

Kadik, A.A., Koltashev, V.V., Kryukova, E.B., Plotnichenko, V.G., Tsekhonya, T.I., and Kononkova, N.N. (2015) Solubility of nitrogen, carbon, and hydrogen in FeO-Na_2O-Al_2O_3-SiO_2 melt and liquid iron alloy: Influence of oxygen fugacity. Geochemistry International, 53, 849–868.

Kadik, A.A., Koltashev, V.V., Kryukova, E.B., Tsekhonya, T.I., and Plotnichenko, V.G. (2016) Application of IR and Raman Spectroscopy for the Determination of the Role of Oxygen Fugacity in the Formation of N–C–O–H Molecules and Complexes in the Iron-Bearing Silicate Melts at High Pressures. Geochemistry International, 54, 1175–1186.

Kowal, A.T. (2002) Anharmonic, vibrational spectra of hydroxylamine and its ^{15}N, ^{18}O, and deuterium substituted analogs. Spectrochimicia Acta, 58, 1055–1067.

Li, Y., Wiedenbeck, M., Shcheka, S., and Keppler, H. (2013) Nitrogen solubility in upper mantle minerals. Earth and Planetary Science Letters, 377- 378, 311–323.

Li, Y., Huang, R., Wiedenbeck, M., and Keppler, H. (2015) Nitrogen distribution between aqueous fluids and silicate melts. Earth and Planetary Science Letters, 411, 218–228.

Li, Y., Dasgupta, R., Tsuno, K., Monteleone, B., and Shimizu, N. (2016a) Carbon and sulfur budget of the silicate Earth explained by accretion of differentiated planetary embryos. Nature Geoscience, 9, 781–785.

Li, Y., Marty, B., Shcheka, S., Zimmermann, L., and Keppler, H. (2016b) Nitrogen isotope fractionation during terrestrial core-mantle separation. Geochemical Perspectives Letters (2016) 2, 138–147.

Libourel, G., Marty, B., and Humbert, F. (2003) Nitrogen solubility in basaltic melt. Part I. Effect of oxygen fugacity. Geochimica et Cosmochimica Acta, 67, 4123–4135.

Mallik, A., Li, Y., and Wiedenbeck, M. (2018) Nitrogen evolution within the Earth's atmosphere–mantle system assessed by recycling in subduction zones. Earth and Planetary Science Letters, 482, 556–566.

Marty, B. (2012) The origins and concentrations of water, carbon, nitrogen and noble gases on Earth. Earth and Planetary Science Letters, 313, 56–66.

Mills, R.D., Simon, J.I., Alexander, C.M.O'D., Wang, J., and Hauri, E.H. (2017) Water in alkali feldspar: the effect of rhyolite generation on the lunar hydrogen budget. Geochemical Perspectives Letters, 3, 115–123.
Miyazaki, A., Hiyagon, H., Sugiura, N., Hirose, K., and Takahashi, E. (2004) Solubilities of nitrogen and noble gases in silicate melts under various oxygen fugacities: implications for the origin and degassing history of nitrogen and noble gases in the Earth. Geochimica et Cosmochimica Acta, 68, 387–401.
Mosenfelder, J.L., and Rossman, G.R. (2013) Analysis of hydrogen and fluorine in pyroxenes: part II. Clinopyroxene. American Mineralogist, 98:1042–1054.
——— (2014) Matrix Effects in SIMS Analysis of Hydrogen in Nominally Anhydrous Minerals (NAMs). American Geophysical Union, Fall Meeting 2014, abstract V41A-4763.
Mosenfelder, J.L., Le Voyer, M., Rossman, G.R., Guan, Y., Bell, D.R., Asimow, P.D., and Eiler, J.M. (2011) Analysis of hydrogen in olivine by SIMS: evaluation of standards and protocol. American Mineralogist, 96, 1725–1741.
Mosenfelder, J.L., Rossman, G.R., and Johnson, E.A. (2015) Hydrous species in feldspars: a reassessment based on FTIR and SIMS. American Mineralogist, 100, 1209–1221.
Mulfinger, H.O. (1966) Physical and chemical solubility of nitrogen in glass melts. Journal of the American Ceramic Society, 49, 462–467.
Mysen, B.O., and Fogel, M.L. (2010) Nitrogen and hydrogen isotope compositions and solubility in silicate melts in equilibrium with reduced (N+H)-bearing fluids at high pressure and temperature: effects of melt structure. American Mineralogist, 95, 987–999.
Mysen, B.O., Yamashita, S., and Chertkova, N. (2008) Solubility and solution mechanisms of NOH volatiles in silicate melts at high pressure and temperature—amine groups and hydrogen fugacity. American Mineralogist, 93, 1760–1770.
Nakamoto, K. (2009a) Infrared and Raman Spectra of Inorganic and Coordination Compounds, Part A: Theory and applications in inorganic chemistry, 419p. Wiley.
——— (2009b) Infrared and Raman Spectra of Inorganic and Coordination Compounds, Part B: Applications in coordination, organometallic, and bioinorganic chemistry, 408p. Wiley.
Raudsepp, M. (1995) Recent advances in the electron-probe micro-analysis of minerals for the light elements. Canadian Mineralogist, 33, 203–218.
Regier, M.E., Hervig, R.L., Myers, M., Roggensack, K., and Wilson, C.N. (2016) Analyzing nitrogen in natural and synthetic silicate glasses by secondary ion mass spectrometry. Chemical Geology, 447, 27–39.
Roskosz, M., Mysen, B.O., and Cody, G.D. (2006) Dual speciation of nitrogen in silicate melts at high pressure and temperature: an experimental study. Geochimica et Cosmochimica Acta, 70, 2902–2918.
Roskosz, M., Bouhifd, M.A., Jephcoat, A.P., Marty, B., and Mysen, B.O. (2013) Nitrogen solubility in molten metal and silicate at high pressure and temperature. Geochimica et Cosmochimica Acta, 121, 15–28.
Schwerdtfeger, K., Fix, W., and Schubert, H.G. (1978) Solubility of nitrogen and carbon in $CaO-SiO_2-Al_2O_3$ slag in presence of graphite at 1450°C. Ironmaking and Steelmaking, 2, 67–71.
Singer, B.S., Jicha, B.R., Fournelle, J.H., Beard, B.L., Johnson, C.M., Smith, K.E., Greene, S.E., Kita, N.T., Valley, J.W., Spicuzza, M.J., and Rogers, N.W. (2014) Lying in wait: deep and shallow evolution of dacite beneath Volcán de Santa María, Guatemala. In A. Gómez-Tuena, S.M. Straub, and G.F. Zellmer, Eds., Orogenic Andesites and Crustal Growth, 385, p. 209–234. Geological Society, London, Special Publications.
Smith, B. (1999) Infrared spectral interpretation: a systematic approach, 265p. CRC Press, Boca Raton, Florida.
Soignard, E., and McMillan, P.F. (2004) Raman Spectroscopy of γ-Si_3N_4 and γ-Ge_3N_4 Nitride Spinel Phases Formed at High Pressure and High Temperature: Evidence for Defect Formation in Nitride Spinels. Chemistry of Materials, 16, 3533–3542.
Solomon, G.C., and Rossman, G.R. (1988) NH^{4+} in pegmatitic feldspars from the southern Black Hills, South Dakota. American Mineralogist, 73, 818–821.
Stanley, B.D., Hirschmann, M.M., and Withers, A.C. (2011) CO_2 solubility in Martian basalts and Martian atmospheric evolution. Geochimica et Cosmochimica Acta, 75, 5987–6003.
——— (2014) Solubility of C-O-H volatiles in graphite-saturated martian basalts. Geochimica et Cosmochimica Acta, 129, 54–76.
Steele, I.M., Hervig, R.L., Hutcheon, I.D., and Smith, J.V. (1981) Ion microprobe techniques and analyses of olivine and low-Ca pyroxene. American Mineralogist, 66, 526–546.
Stolper, E. (1982) Water in silicate glasses: an infrared spectroscopic study. Contributions to Mineralogy and Petrology, 81, 1–17.
Sugiura, N. (1998) Ion probe measurements of carbon and nitrogen in iron meteorites. Meteoritics and Planetary Science, 33, 393–409.
Tenner, T.J., Hirschmann, M.M., Withers, A.C., and Hervig, R.L. (2009) Hydrogen partitioning between nominally anhydrous upper mantle minerals and melt between 3 and 5 GPa. Chemical Geology, 262, 42–56.
Van der Heide, P. (2014) Secondary Ion Mass Spectrometry, 365p. Wiley.
Von der Handt, A. and Dalou, C. (2016) Quantitative EPMA of nitrogen in silicate glasses. Microscopy and Microanalysis 22 (S3), 1810–1811.
Watenphul, A., Wunder, B., and Heinrich, W. (2009) High-pressure ammonium-bearing silicates: Implications for nitrogen and hydrogen storage in the Earth's mantle. American Mineralogist, 94, 283–292.
Watenphul, A., Wunder, B., Wirth, R., and Heinrich, W. (2010) Ammonium-bearing clinopyroxene: a potential nitrogen reservoir in the Earth's mantle. Chemical Geology, 270, 240–248.
Williams, L.B., Clauer, N., and Hervig, R.L. (2012) Light stable isotope microanalysis of clays in sedimentary rocks. In P. Sylvester, Ed., Quantitative mineralogy and microanalysis of sediments and sedimentary rocks. Mineralogical Association of Canada Short Course, 42, 55–73.
Williams, L.B., Środoń, J., Huff, W.D., Clauer, N., and Hervig, R.L. (2013) Light element distributions (N, B, Li) in Baltic Basin bentonites record organic sources. Geochimica et Cosmochimica Acta, 120, 582–599.
Williams, P. (1979) The sputtering process and sputtered ion emission. Surface Science, 90, 588–634.
Wohlers, A., and Wood, B.J. (2015) A Mercury-like component yields U in the core and high mantle ^{142}Nd. Nature, 520, 337–340.
Yokochi, R., Marty, B., Chazot, G., and Burnard, P. (2009) Nitrogen in peridotite xenoliths: Lithophile behavior and magmatic isotope fractionation. Geochimica et Cosmochimica Acta, 73, 4843–4861.
Yoshioka, T., Wiedenbeck, M., Shcheka, S., and Keppler, H. (2018) Nitrogen solubility in the deep mantle and the origin of Earth's primordial nitrogen budget. Earth and Planetary Science Letters, 488, 134–143.
York, D. (1966) Least-squares fitting of a straight line. Canadian Journal of Physics, 44, 1079–1086.
Zinner, E., Ming, T., and Anders, E. (1989) Interstellar SiC in the Murchison and Murray meteorites: isotopic composition of Ne, Xe, Si, C, and N. Geochimica et Cosmochimica Acta, 53, 3273–3290.
Zolotov, M.Y. (2010) On the chemistry of mantle and magmatic volatiles on Mercury. Icarus, 212, 24–41.

Manuscript received March 1, 2018
Manuscript accepted September 7, 2018
Manuscript handled by Adam Kent

Endnote:

[1]Deposit item AM-19-16533, Supplemental Material. Deposit items are free to all readers and found on the MSA website, via the specific issue's Table of Contents (go to http://www.minsocam.org/MSA/AmMin/TOC/2019/Jan2019_data/Jan2019_data.html).